# THREE-DIMENSIONAL FOURIER ANALYSIS OF ELECTRON MICROSCOPY TO CHARACTERIZE DIFFUSION TENSOR IMAGING DATA

Kaveh Nik Jamal


Master´s thesis

Åbo Akademi University

Faculty of Science and Engineering

1.11.2016

Master´s degree in Biomedical Imaging

Credits: 45 ECTS

Specialization theme:

Mathematics, image processing

using Matlab

Supervisors :

1. Alejandra Sierra, PhD.
2. Raimo Salo, M.Sc.

Examiners:

1. Olli Gröhn, PhD.
2. Joanna Huttunen, PhD.

Åbo Akademi University

Department of Biosciences

Faculty of Science and Engineering

Kaveh Nik Jamal, knikjama@abo.fi , matriculation number: 38126

Three-Dimensional Fourier Analysis of Electron Microscopy to Characterize Diffusion Tensor Imaging Data

Master´s thesis, 67 pp, 1 Appendix

MASTER OF SCIENCE

October 2016

*Abstract*

Diffusion tensor imaging (DTI) is a highly sensitive MRI method that unveils the changes in brain microstructures. By estimating the movement of protons through different areas of complexity in the brain, DTI provides a remarkable contrast between white matter and grey matter fibers three-dimensionally (3D), as tissues differ in causing restriction to the movement of water protons. Particularly after neuropathology, DTI reveals significant changes in the measured parameters. However, the contrast provided by DTI, reflecting the organization of fibers is not clearly understood. In addition, there has been a gap thus far, in direct characterization of DTI due to limitations in planar images of histology. In this work, we first improved the two-dimensional (2D) histological characterization of DTI data. 2D Fourier analysis was applied to the digital photomicrographs of myelin and GFAP stainings in order to probe the changes that occur after status epilepticus in rats. It revealed a significant change in the fiber orientations and anisotropy after status epilepticus as compared to the controls in the CA3b region in the hippocampus, concurring with DTI results. With the aim of providing the third-dimension to the histological characterization, we implemented Fourier analysis in stacks of serial block face scanning electron microscopy (SBEM). It gives a distinct advantage of providing all the obstacles (membranes) for the water diffusion. Consequently, we obtained anisotropy and orientation for the grey and white matter in 3D at

the same level of DTI voxels. After traumatic brain injury, we observed a remarkable decrease in 3D anisotropy, ipsilaterally to the injury both in the cortex and external capsule. This decrease was associated with an increase in the number of reactive astrocytes and axonal damage. The development of a novel method for 3D Fourier analysis of SBEM is the first step in the validation of DTI data for future studies focused on detecting the changes in brain tissue after pathological conditions.

*Key words*: anisotropy, DTI, three-dimensional Fourier analysis, GFAP, grey matter, myelin, myeloarchitecture, fiber orientations, SBEM, white matter.

**Abbreviations**

| | |
|---|---|
| AI | anisotropy |
| DTI | Diffusion Tensor Imaging |
| FA | fractional anisotropy |
| GFAP | glial fibrillary acidic protein |
| MRI | Magnetic Resonance Imaging |
| ROI | region of interest (two-dimensional) |
| SBEM | serial block-face scanning electron microscopy |
| TBI | traumatic brain injury |
| 2D-FT | two-dimensional Fourier transformation |
| 3D-FT | three-dimensional Fourier transformation |

VOI volume of interest (three-dimensional)

## Contents

# 1. INTRODUCTION

## *1.1. Background*

The brain is the control center of the body. It is a highly complex organ, both functionally and structurally. The fundamental element of the brain is the neuron. A neuron is responsible for encoding and transferring the information by firing electrical signals in reaction to various stimuli (Bear et al., 2007). From the body of the neuron, dendrites and axons are projected three-dimensionally (Longstaff, 2000). Axons are responsible for transferring information over long distances by creating synapses to other neurons. Dendrites are the branches projected from the neuron body, with specialized membranes incorporating receptors for the detection of neurotransmitters. Among others, glial cells are another type of cells in the brain, estimated to be ten times superior in numbers compared to the neurons (Longstaff, 2000). There are several types of glial cells. Astrocytes form the majority of the glial cells in the brain, providing support to the neurons. They are located between neurons and also between neurons and vessels. Microglial cells assist the brain by providing immune support to the neurons and their vicinity (Bear et al., 2007). Oligodendrocytes, another type of glial cells create insulation for the axons by spiraling them with myelin sheaths (Levitan and Kaczmarek, 2002). Bundles of the myelinated axons together form the white matter. The grey matter, by contrast, is predominantly composed of cell bodies. Hence, the brain embraces a sophisticated structure constituted upon various levels of cellular components.

Neurodegenerative diseases leave their marks on function and structure in the brain which can be uncovered by neuroimaging techniques. Early detection of the brain pathology is essential for prompt interventions and therapeutic measures by neurologists and healthcare professionals. One example of the neuropathology is the Alzheimer's disease (AD). Patients with AD have significant neurodegeneration of the cortex and subcortical structures. One specific feature of AD is the presence of diffuse plagues, encircled by neurodegenerative neurites and glial cells. Another example is the multiple sclerosis (MS) which is a demyelinating disease affecting white matter (Filippi et al., 2012). MS is caused by the immune system attacking the proteins which myelin is made from, leading to destruction of the myelin sheaths. Epilepsy is one more instance of pathology, involving the recurrent

seizures associated with the abnormal firing of neurons. The factors causing epilepsy may include traumatic brain injury, genetic inheritance, and even alcohol withdrawal. Epilepsy could inflict structural abnormalities in cell count and organization in specific brain regions. Traumatic brain injury is a significant cause of disability and death affecting millions of people worldwide. Diffuse axonal injury (DAI) is one of the most common neuropathological consequences of trauma in the white matter, ranging from focal disruptions of axons to total neural degeneration. At microscopic levels, DAI can impose damage in the molecular transport of axons, initiate neuroinflammation and eventually disruption of axons (Husain and Scott, 2016). In addition, a recurrent loss in the brain volume has been found in grey matter as a consequence of post trauma pathology (Benson et al., 2012). For detecting these alterations in the brain during the above mentioned pathological processes and many others, neuroimaging techniques have been developed and constantly improved. Computed Tomography (CT) is one of the primary tools for diagnosing the previously mentioned injuries. CT has limited contrast for soft tissue and is highly restricted in the detection of microscopic-level alterations in brain structures, particularly axon fibers. Positron Emission Tomography (PET) provides information about the function and metabolism of the brain by detecting the gamma rays generated from annihilation of the positrons with the electrons. Although it is a very useful tool for monitoring the metabolisms and molecular activity in the brain over time, the spatial resolution provided by PET is relatively low.

Magnetic resonance imaging (MRI) techniques are capable of revealing anatomy, function, and metabolism of the brain (Kinnunen et al., 2010). Through using pulsed radio frequencies for nuclear magnetic resonance, this technique is not harmful to living cells compared to ionizing radiation of CT or PET. Conventional MRI methods are already widely used in clinics and research used in diagnosis and prognosis of diseases. T1- or T2-weighted, proton density, or diffusion MRI create a broad spectrum of mechanisms of contrast which makes MRI a highly versatile imaging technique. Particularly in neurology, MRI provides excellent contrast between white matter and grey matter of the brain tissue with submillimeter resolution, allowing a more detailed probe compared to CT or PET (Tardif et al., 2016).

Yet, conventional MRI often fails in detecting more subtle microstructural alterations in the brain, which can be used as markers for neurodegenerative diseases. Novel and more advanced MRI techniques, such as diffusion tensor imaging and susceptibility weighted imaging among others, have been implemented in recent years. Such new approaches are likely to open completely new windows for detecting pathological changes in the brain, and establishing noninvasive reliable markers for disease diagnosis and progression.

### *1.2. DTI, the method of choice to infer tissue microstructure*

#### 1.2.1. Diffusion tensor modelling

Diffusion tensor imaging (DTI) is a method among MRI techniques which is capable of determining the microstructural alterations in the white matter and also grey matter (Andrade et al., 2014). This is due to the versatility of magnetic resonance imaging, which can be made sensitive to the movement of water. Water molecules randomly diffuse through the biological matter between two particular spatial locations. While the primary cause of the diffusion process is the thermal fluctuations, it is also modulated by interactions of the water molecule with cellular and subcellular membranes, including the organelles (Alexander et al., 2007). Diffusion can take place in, out, through or around the various cellular components of these structures. Each element of the whole brain MRI image is a three-dimensional cube, referred to as “voxel”. Each voxel embodies a considerable volume of microstructures that will cause resistance for free movement of a water molecule. The general concept of the diffusion imaging technique includes fitting to a Gaussian model in order to extract a diffusion map, which is subsequently put into a tensor model for each individual voxel throughout the whole MRI image (Mori and Tournier, 2014). In practice, this is achieved by imposing strong pulses by the gradient coils of MRI scanners, which is the essential process for sensitizing MRI to diffusion.

The application of the tensor model for diffusion measurements was presented by Basser and colleagues as a multivariate normal distribution as a function of displacement ($r$) and time ($t$) (Basser et al., 1994):

$$P(\Delta\vec{r}, \Delta t) = \frac{1}{\sqrt{(4\pi.\ \Delta t)^3 |D|}}\ exp\left\{\frac{-\Delta\vec{r}^T.\ D^{-1}.\ \Delta\vec{r}}{4\,\Delta t}\right\}$$

In which the diffusion tensor is included as a covariance matrix of diffusion displacements normalized three-dimensionally:

$$D = \begin{bmatrix} \boldsymbol{D_{xx}} & D_{xy} & D_{xz} \\ D_{yx} & \boldsymbol{D_{yy}} & D_{yz} \\ D_{zx} & D_{zy} & \boldsymbol{D_{zz}} \end{bmatrix}$$

where the diagonal elements (in bold) are the variances in diffusion measurements along the *x*,*y* and *z* axes and off-diagonal elements of this matrix are the covariance terms which are symmetrical based on the diagonal elements ($D_{ij} = D_{ji}$). Subsequently, this matrix is mathematically diagonalized in order to yield three eigenvalues ($\lambda_1, \lambda_2, \lambda_3$) and three eigenvectors ($\vec{e}_1, \vec{e}_2, \vec{e}_3$). The diffusion tensor can be visualized for each voxel by an ellipsoid with a volume and a direction. The eigenvalues define the radii for this ellipsoid and the eigenvectors indicate the directions of the principal axes (Rodriguez and Concha, 2015). The diffusion ellipsoid shows the overall dominant diffusion direction at each voxel in MRI. Generally, several diffusion maps are acquired by imaging over different directions and averaged, which can be further analyzed for quantification purposes (Nilsson et al., 2013).

### 1.2.2. Anisotropy and orientation

Fractional anisotropy (FA) is a DTI quantity reflecting the degree of homogeneity of the tissue microstructures. FA was initially developed by Moseley and coworkers for understanding the demyelination disorders in the white matter (Moseley et al., 1991). FA is basically the degree of variance between three eigenvalues (λ) from the covariance matrix [D]:

$$FA = \sqrt{\frac{3}{2}} \frac{\sqrt{(\lambda_1 - \bar{\lambda})^2 + (\lambda_2 - \bar{\lambda})^2 + (\lambda_3 - \bar{\lambda})^2}}{\sqrt{{\lambda_1}^2 + {\lambda_2}^2 + {\lambda_3}^2}}$$

in which the mean diffusivity is:

$$\bar{\lambda} = \frac{\lambda_1 + \lambda_2 + \lambda_3}{3}$$

FA is a scalar value between zero and one, zero for isotropic diffusion and 1 for anisotropic diffusion. In order to understand the concept of anisotropy, one should know the process of diffusion for a water molecule in the biological media. For instance, in the compact pattern of white matter fibers, such as the genu of the corpus callosum, the cell membranes including

axonal myelin sheaths cause impediment to the water diffusion more remarkably across their length, compared to the parallel direction (Fig.1). In other words, the water diffusion is significantly lower (more anisotropic) in perpendicular direction to the fibers. As a result, in DTI images, the corpus callosum is far brighter compared to a conventional MRI, because the water molecules cannot flow freely in perpendicular pathways to these fibers. This specific phenomenon is translated into anisotropic diffusion.

On the other hand, in isotropic media such as the spinal fluid, there is no restriction for diffusion of water in any possible direction. As a result, the diffusion will be isotropic and consequently the diffusion profile will be in a spherical shape. An example of isotropic diffusion in the brain is the grey matter fibers. With the presence of crossing fibers, the water molecules go through approximately similar displacements among all directions. This is

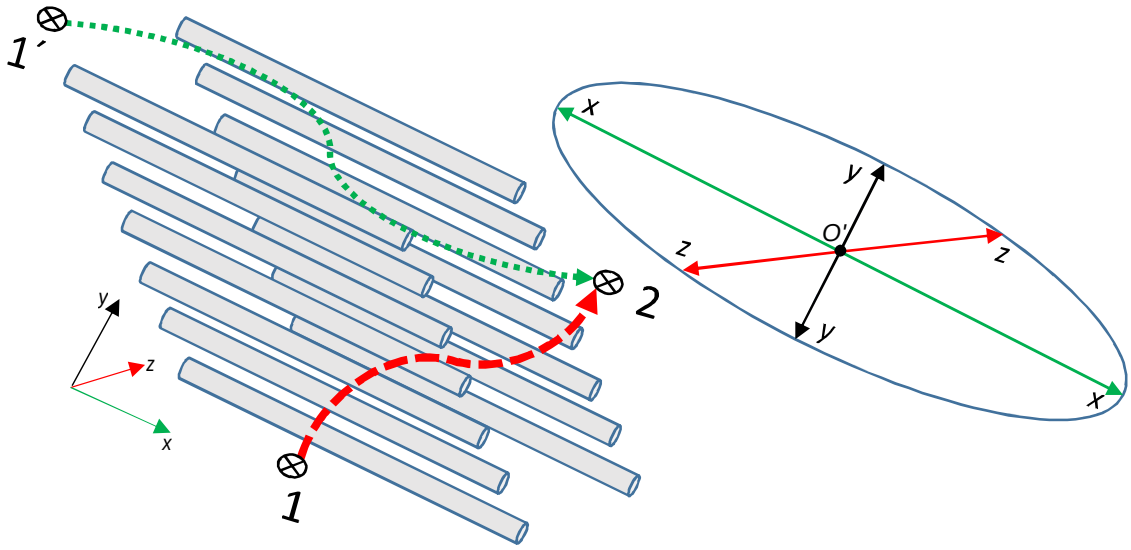


Fig.1. 3D visualization of the diffusion tensor by an ellipsoid. *Left)* The homogeneous, parallel organization of the packed fibers in white matter, for example the genu of the corpus callosum. Each tubular shape shows a myelinated axon. These uniformly orientated bundles restrict the diffusion of water more significantly, perpendicularly to their directionality (*z* direction, marked in red). Thus, the movement of a water molecule through the uniform packed fibers, from point 1 to point 2 (red dashed arrow), is highly hindered due to the existence of bundles (*z* direction). However, in parallel to the directionality of the same fibers (*x* direction), a water molecule can diffuse far more easily from point (1´) to point (2) (green arrow), with less resistance because of the inter-tubular space between the bundles. *Right)* The diffusion tensor model for the same molecule through the same (white matter) fiber bundles (*left*) in all three dimensions: *x* (green), *y* (black) , *z* (red), originating from the center of the ellipsoid (O´) as the reference point. This ellipsoid is an indication of a highly anisotropic diffusion of water molecule perpendicular to the direction of fibers in the left side.

similar to a more isotropic diffusion, the characteristics of a free and unrestricted movement of water molecules (Beaulieu, 2002). For instance, in an early study of anisotropy by Moseley and colleagues found that in the white matter of cat brain and spinal cord, water diffusion is anisotropic while in the grey matter it is more isotropic (Moseley et al., 1990).

### 1.2.3. The need for in-depth DTI quantifications

Anisotropy corresponds to the changes in the coherent microscopic organization at the cellular scale (Basser and Pierpaoli, 1996). DTI has revealed reductions of fractional anisotropy in the corpus callosum and external capsule of patients with traumatic brain injury, a phenomenon which cannot be detected by conventional MRI (Xu et al., 2007; Rutgers et al., 2008; Matsushita et al., 2011).

Despite all the studies using DTI in normal and pathological conditions, the contrast provided by DTI is not fully understood. A decreased fractional anisotropy is believed to indicate the loss of tissue integrity, a significant tool in exhibiting the white matter anatomy (Werring et al., 1998). It is also believed to be reflecting axonal and myelin injury in the white matter. Thus, a reduction in anisotropy may indicate degradation in the directional organization among the fibers which are considered as barriers to the water diffusion (Beaulieu, 2002). An increase in FA could be revealing axonal regeneration and plasticity (Budde et al., 2011). Furthermore, if a voxel contains single fiber directionality (see Fig.1) the tensor model is accurate for diffusion characterization (Basser et al., 1994). Thus, the directional dependence of DTI anisotropy can be fully quantified by the diffusion tensor, solely when the diffusion process has spatially homogenous increments, as in the corpus callosum (Frank, 2002). Moreover, alongside other conventional diffusion MRI techniques, DTI makes an average of the random movements of water molecules regardless of the exchange between intra- and extracellular features (Basser and Jones, 2002). Among several directions, DTI generates a diffusion tensor from the apparent diffusion coefficient of the water molecules (Assaf and Basser, 2005). This coefficient could be measured in parallel and perpendicular directions to the homogeneous fiber packs, ensuing immense discrepancies in the white matter (Basser and Jones, 2002). Although white matter contains a homogenous tubular structure, it also encompasses other cells whose membranes can be a factor for altering the diffusion after pathology. It is believed that changes in the intrinsic characteristics of the fibers and their varying angular distributions in a voxel may lower the anisotropy in DTI (Anderson, 2005).

### *1.3. Histological characterization of DTI and its limitations*

For studying the cellular components that assumingly contribute to the changes in fractional anisotropy and orientation, various histological stainings have been used (Mac Donald et al., 2007; Mädler et al., 2008; Li et al., 2011; Seehaus et al., 2015). Furthermore, long-term quantification of DTI by exploring the histopathology of epileptogenesis are of paramount necessity (van Eijsden et al., 2011). For example, after epilepsy and traumatic brain injury, the astrocytes (Fig.2A) are believed to have a role in helping to preserve the tissue by increasing their domains. Such changes among these star-shaped cells can be revealed by the GFAP immunostaining since the growth of astrocytes is associated with increased expression of this protein. In addition, the regrowth of astrocytes may not be limited to a planar domain. As shown in Fig. 2, there are some structures which are in plane, while others are perpendicular to the field of view and not considered in 2D analysis of the conventional histological preparations. For this reason, planar histology not only lacks all the barriers influencing the water diffusion within the tissue, but also the 3$^{rd}$ dimension that facilitates a correlation with the 3D voxels of DTI.

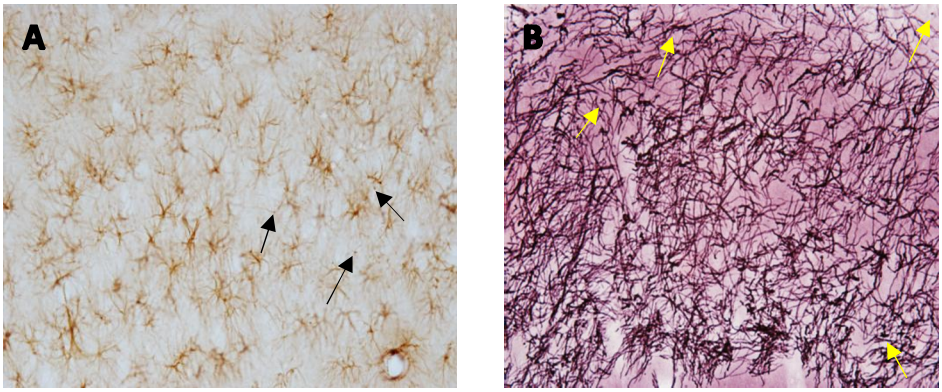


Fig.2. The limitations of planar histology. (A) GFAP-stained section showing astrocytes in the CA3b in the hippocampus of the rat brain. (B) Myelin-stained section of the same region which shows myelinated axons. Arrows indicate some features which are mostly perpendicular to the field of view. Therefore a three-dimensional histological approach is needed to be able to compare with 3D DTI data.

#### 1.3.1. Fourier analysis in 2D

In mathematics, a two-dimensional image can be represented as a function, *f(x,y)*. If we assume the magnitude of the image in *x* direction is M, and in y direction is N, the image can be viewed as a matrix with M rows and N columns. Fourier transformation decomposes an image to its sine and cosine components. The input of transformation is the image in the

spatial domain *f(x,y)*, and the output is the Fourier image, the frequency domain *F(u,v)*. For digital images, it is sufficient to have a discrete Fourier transform that includes only the most relevant set of frequencies sufficient to represent the spatial image:

$$F(u,v) = \sum_{x=0}^{M-1}\sum_{y=0}^{N-1} f(x,y)e^{-i2\pi\left(\frac{ux}{M}+\frac{vy}{N}\right)}$$

where $i = \sqrt{-1}$ .

For DTI quantification, cell membranes are particularly the most important target due to causing restriction for diffusion of water protons. Having the image transformed in frequencies by Fourier, it is possible to specifically take into account the frequencies representing the membranes by means of singular value decomposition of the Fourier image. Budde and collaborators recently used the above mentioned concept for exhibiting the intelligible organization of white matter as well as grey matter (Budde et al., 2011). They applied Fourier transformation to the images of Dil-stained sections to investigate the microstructural changes after TBI in the rats. Dil (1,1'-Dioctadecyl-3,3,3',3'-Tetramethylindocarbocyanine Perchlorate) is a lipophilic membrane stain which diffuses laterally to stain the whole cell and is used to reveal cellular membranes and lipids in neural tracking. However, this method lacked the 3rd dimension because the histological preparations were still two dimensional. Moreover, several stainings were necessitated after Dil staining in order to understand which microstructures contributed the most to DTI data. In each DTI voxel, there are numerous fiber structures that contribute to the analysis output, for which conventional histology may not be sufficient to quantify. Furthermore, the necessity of multiple histological stainings for correlating the data with DTI is a challenge to be dealt with. On the other hand, various sorts of cells and fibers have different impacts on tissue properties based on their organization (Marquez, 2006).

### 1.3.2. Microscopy methods used for providing the 3rd dimension

There are several histological methods which could overcome the problem of the missing 3rd dimension by incorporating *z* stacks using confocal or multi-photon microscopy (Axer and Keyserlingk, 2000; Napadow et al., 2001; Jespersen et al., 2012; Schrauwen et al., 2012; Khan et al., 2015; Kullkarni et al., 2015; Petroll et al., 2015). This could be applied to Dil

staining or other specific markers, to obtain the 3rd dimension that may aid for further validation studies (Axer et al., 1999). Most recently, full characterization of the fiber orientations has also been conducted by stacking histological images using confocal microscopy, combined with the structure tensor analysis (Schilling et al., 2016). Among others, 3D-polarized light imaging has also been exploited to obtain unit vectors which reveal the voxel-wise fiber tract orientations, found on the birefringent characteristics of the myelin sheaths (Axer et al., 2011 a; Reckfort et al., 2015). The lipid membrane of myelin makes the light elliptically polarized and turns it into a direct tool for measuring 3D spatial orientation of axons (Axer et al., 2011 b). Thus, it has the capability to probe the long range and single fibers in a scale from macroscopic to microscopic range (Menzel et al., 2015). Although these methods provide the 3rd dimension, they are still restricted to specific stainings for the targeted histopathological substrates as the subject of the study. Uneven staining and alignment problems are common limitations to these methods.

### *1.4. Electron microscopy containing all diffusion barriers three-dimensionally*

The necessity of evaluating the tissue organization by optical or electron microscopy has been proven to be indispensable for the direct visualization of cellular and subcellular structures (Budde and Annese, 2013). Among various areas of the brain, neural fibers constitute a highly dense and complex network which causes a significant challenge for unveiling their structure. All the structural components of axons are longitudinally oriented that can be barriers to water diffusion perpendicular to the length of axons (Beaulieu, 2002). Hence, the influence of cell membranes including myelin sheaths on anisotropy must be scrutinized. Moreover, a typical voxel in diffusion MRI experiments ranges about 10 $mm^3$ (Fig.3A) enclosing numerous cells and tissue components (Assaf and Basser, 2005). One advanced technique that might overcome these problems is serial block face scanning electron microscopy (SBEM). It is an electron microscopy technique which produces stacks of images at a mesoscale level (Denk and Horstmann, 2004) and fills the gap between the high resolution transmission electron microcopy (TEM) and optical microscopy (Zankel et al., 2014). SEM has been a typical method utilized for surface quantification based on the interactions of electron beams with the sample surface (Miranda et al., 2015). Since SEM uses the backscattered electrons from the surface of the specimen for generating images, it is capable of imaging large volumes of tissues in a block-face with nanometer resolution range.

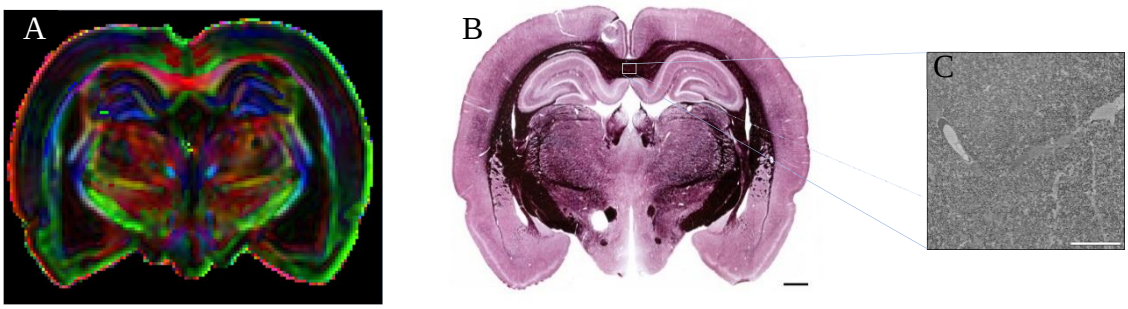


Fig. 3. From voxels to 3D-electron microscopy. (A) Directionally encoded color map of a rat brain. Each square element of this image is a 2D view of a 3D voxel in the whole brain image. For each individual voxel the diffusion tensor estimates a dominant fiber directionality for the whole tissue substructures, exhibited by red, green or blue color. For example, the red color of the corpus callosum indicates that the fiber orientation is medial-lateral. (B) Myelin-stained section of the same animal, only indicating the myelinated axons, while being limited to 2D. (C) One image from a SBEM stack of the corpus callosum in 3D, containing all the membranous structures with a remarkably higher resolution. Scale bar: (B) 1mm and (C) 25 µm. SBEM: serial block face electron microscopy, 2D: two-dimensional, 3D: three-dimensional.

In SBEM, first the face of the tissue sample is imaged, then a microtome included in the chamber cuts a thin section, and subsequently the face is imaged again producing a 3D stack of images in a high resolution. Consequently, it is expected to generate a volume which contains cell bodies, axons, dendrites, organelles and synapses all together. This is owed to the sufficiency of the SBEM resolution for probing the neural connectome and structures (Mikula et al., 2012; Sawai et al., 2013). Due to the use of back-scattered electrons, it also creates an atomic contrast and an inverted image of the sample similar to TEM (Borrett and Hughes, 2016). Contrary to TEM, the problem of data loss and deformation of images does not exist in SBEM, since the block face is scanned after the cutting (Wernitznig et al., 2016). Recent improvements in staining techniques have made the block face preparation less time consuming (Thai et al., 2016). The block face imaging method prevents section distortion and has an improved *Z* resolution (Denk et al., 2012) that is essential for tracking the neural processes over long distances. On the other hand, SBEM provides improved alignment of the sections and its focused beam creates thinner sections, resulting in advanced segmentation (Lichtman et al., 2014). SBEM analysis can provide a direct quantitative comparison between DTI and histological analyses and close the gap in the characterization of pathological substrates. Nevertheless, the enormous data volume of SBEM requires a time efficient and automated analysis method which could be used as a gold standard tool.

# 2. AIMS

### *2.1. Fourier analysis in 2D histology*

In this project, first we will explore the possibilities of 2D-FT analysis in conventional histological stainings. We will investigate the contribution of two different components to water diffusion in control and pilocarpine rats in the corpus callosum, cortex and CA3b of the hippocampus. This can help understand the specific role of each sub-localized membranous structure in contributing to DTI anisotropy, myelin sheaths and astrocyte membranes, by histology. DTI analysis will be performed by a voxel-based approach. Three consecutive voxels will be chosen, analyzed and averaged for each region of interest.

### *2.2. Fourier analysis in 3D electron microscopy*

The main aim of this study is to measure the overall 3D anisotropy and orientations of the dominant tissue structures in the rat brain, contained in a stack of 3D electron microscopic images generated by SBEM and compare the results with DTI data. In these stacks, all the microstructural components or membranous barriers responsible for restricting the water diffusion could be taken into account. It will indeed be a gold standard, direct, and principled method for full characterization of the diffusion tensor imaging, regardless of the various levels of fiber complexity.

The specific aims are:

- to use the already existing 2D-Fourier analysis to analyze white and gray matter areas in the rat brain in normal and pathological conditions.
- to develop 3D-Fourier analysis for the SBEM image stack.
- to analyze 3D-EM data with the novel Fourier analysis for creating anisotropy in 3D, a reliable biomarker tool to probe the changes that occur after neropathology.
- to compare data from 3D-Fourier analysis to DTI data from selected brain areas, in order to scrutinize the fractional anisotropy.

### *2.3. Hypothesis*

We hypothesized that Fourier transformation can be applied to 3D stacks of SBEM and further analyzed by the principal component analysis, with the aim of measuring anisotropy and orientation of the dominant fibers.

## 3. METHODS AND MATERIALS

The flowchart of this project is presented by the following graph (DTI: diffusion tensor imaging 2D: two dimensional, 3D: three dimensional):

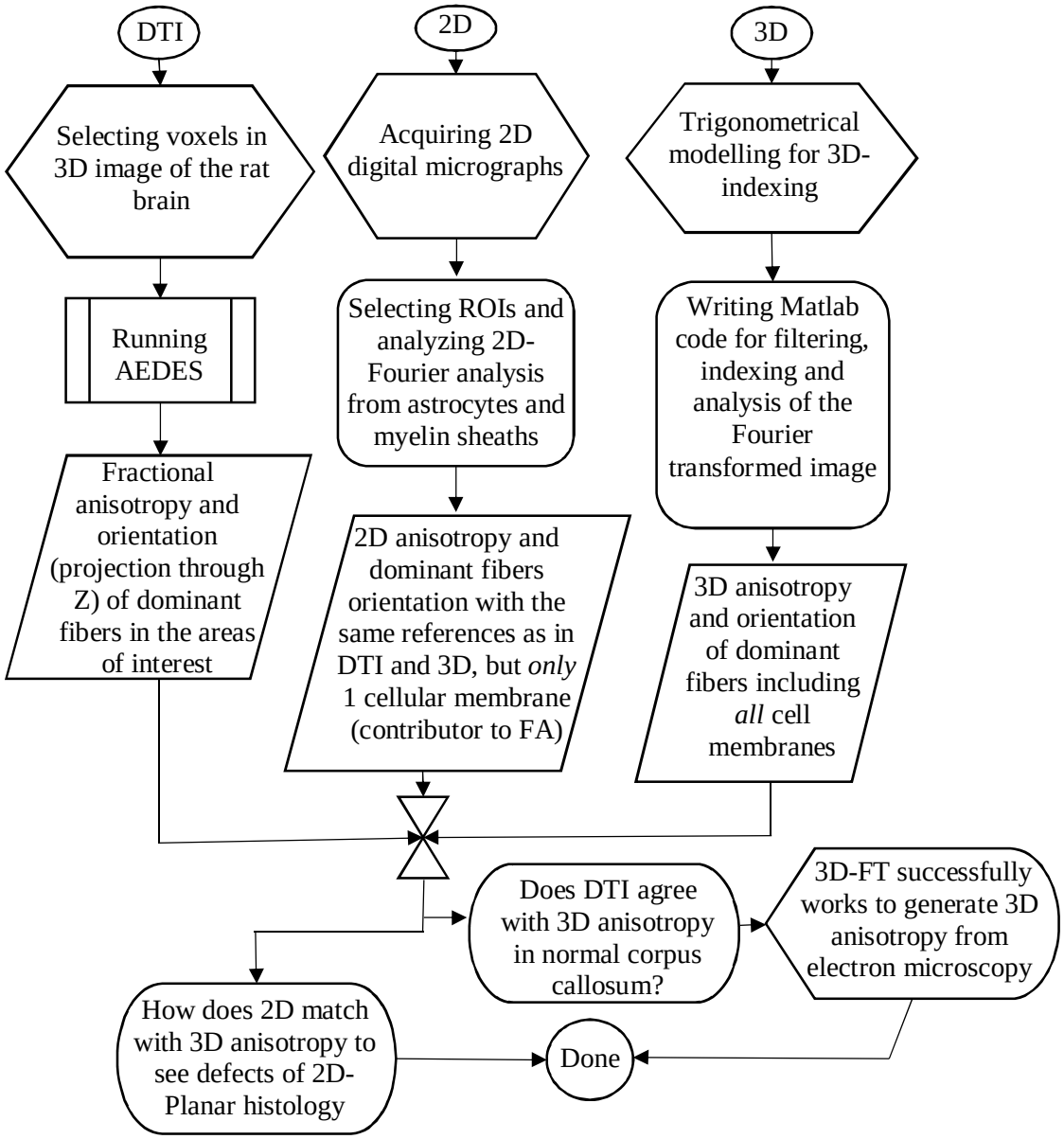


The implementation of the analysis of this work was performed by Matlab software (Math Works, version R 2011a). The 2D and 3D analysis performed for this project involves the discrete Fourier transformation. DTI analysis was done by AEDES (free Matlab toolbox for MRI analysis, http://aedes.uef.fi/).

### *3.1. Experimental animals*

All the animals were housed in individual cages in climate controlled room (22°C ± 1°C) humidity (50% to 60%) with 12 hour light/dark cycle with an ad libitum diet. All animal procedures were approved by the Animal Ethics Committee of the Provincial Government of Southern Finland (for TBI 2008-05812, for epilepsy 2010-05651), and conducted in accordance with the guidelines set by the European Community Council Directives 86/609/EEC.

Status epilepticus was induced in male Wistar rats (10 weeks old, weight 300-350 g, National Laboratory Animal Center Kuopio) (n = 8). They were injected with scopolamine (s.c., 2 mg/kg; #S-8502, Sigma, Chemical Co., St. Louis, MO, USA) for decreasing the peripheral adverse effects of pilocarpine. After thirty minutes, status epilepticus was induced by pilocarpine (i.p., 320 mg/kg, #P-6503, Sigma, Chemical Co., St. Louis, MO, USA). The development of status epilepticus was observed visually for 3 hours and the only animals included in this work were the rats that developed recurrent generalized seizures. Finally, diazepam (i.p., 10 mg/kg, StesolidNovum, Dumex-Alpharma) was administered aimed for curbing the mortality. Age and weight-matched controls received saline (n = 6). Rats were first anesthetized with isoflurane.

TBI was induced using lateral fluid-percussion (LFP) injury model (Kharatishvili et al., 2009) in male Sprague-Dawley rats (10 weeks old, weight 300–350 g, Harlan Netherlands B.V., Horst, Netherlands). Briefly, rats (n = 5) were anesthetized by an injection of a mixture (6 ml/kg, i.p.) containing sodium pentobarbital (58 mg/kg), chloral hydrate (60 mg/kg), magnesium sulfate (127.2 mg/kg), propylene glycol (42.8%), and absolute ethanol (11.6%). A craniotomy of 5 mm in diameter was performed between the bregma and lambda on the left convexity (anterior edge 2.0 mm posterior to the bregma; lateral edge adjacent to the left lateral ridge). LFP injury was induced by a transient (21–23 ms) fluid pulse impact against the exposed dura by using a fluid-percussion device (AmScien Instruments, Richmond, VA). The impact pressure was controlled to 3.2–3.4 atm, to induce severe brain injury. After impact, the dura was checked to ensure it had remained intact. Sham-operated control animals (n = 4) received all surgical procedures except the fluid-percussion impact.

### *3.2. Tissue preparation*

The rats were sacrificed 79 days after status epilepticus or 6 months after TBI for *ex vivo* imaging and histology. The animals were deeply anesthetized with an i.p. injection (7 ml/kg) of solution containing sodium pentobarbital (10 mg/ml), chloral hydrate (10 mg/ml), magnesium sulfate (21.2 mg/ml), propylene glycol (40%), and absolute ethanol (10%) and perfused transcardially with saline for 5 minutes (30 ml/min) followed by 4 % paraformaldehyde in 0.1 M phosphate buffer, pH 7.4 (30 ml/min) for 25 minutes. The brains were removed from the skull and post-fixed in 4% paraformaldehyde for 4 h.

### *3.3. Ex vivo diffusion tensor imaging*

Prior to *ex vivo* MRI, the brains were washed and stored in 0.9% NaCl until imaging. During *ex vivo* scanning, all the brains were immersed in perfluoropolyether (Solexis Galden®, Solvay, USA) to avoid signal from the solution. *Ex vivo* DTI experiments were carried out in a vertical 9.4 T magnet (Oxford Instruments PLC, Abingdon, UK) interfaced to a Varian Direct Drive console (Varian Inc., Palo Alto, CA) using a quadrature volume radiofrequency-coil (diameter 20 mm, Rapid Biomedical GmbH, Rimpar, Germany) for transmitting and receiving. High-resolution 3D data sets were acquired using a 3D spin echo sequence (TR = 1.0 s, TE = 30 ms, $\delta$ = 5 ms, $\Delta$= 17 ms and b-value = 1000 s/mm$^2$) with 6 diffusion weighting directions and one without diffusion weighting. The field-of-view (FOV) was 29.3 × 16.5 × 13.7 mm$^3$ covered with a 256 × 72 × 60 points (data resolution of 114 × 229 × 228 μm$^3$) zero padded to 256 × 144 × 120 points resulting in an interpolated spatial resolution of 114 × 114 × 114 μm$^3$. Total scan time was approximately 16 hours.

### *3.4. Histological procedures*

After *ex vivo* imaging, the brains were washed out in 0.9% NaCl for at least for 2 h at 4°C, and then placed in a cryoprotective solution containing 20% glycerol in 0.02 M potassium phosphate-buffered saline (KPBS; pH 7.4) for 36 h. The brains were frozen in dry ice and stored at -70 °C until cutting. Sectioning was done in the horizontal plane (30 μm thick sections into 1-in-5 series) using a sliding microtome. The first series of sections was stored in 10% formalin at room temperature, and the remaining series in a cryoprotectant tissue-collecting solution (30% ethylene glycol, 25% glycerol in 0.05 M sodium phosphate buffer) at -20°C until processed.

The second series of sections were stained for myelin. First, sections were mounted on gelatin-coated slides and dried at 37°C. They were then incubated in a 0.2% gold chloride solution ($HAuCl_4 \bullet 3H_2O$, G-4022 Sigma) in 0.02 M sodium phosphate buffer (pH 7.4) containing 0.09% NaCl for 11–14 h at room temperature in the dark. The slides were then washed twice for 4 min in 0.02 M sodium phosphate buffer in 0.09% NaCl and placed in a 2.5% sodium thiosulfate solution for 5 min. After three 10 min washes in the buffer solution, sections were dehydrated through an ascending series of ethanol, cleared in xylene and cover slipped with DePeX (BDH, Laboratory Supplies, Dorset, UK).

Sections from the third series (3 sections per animal) were immunohistochemically stained with astroglial marker, GFAP. Sections were washed three times with 0.02 M KPBS (10 min each) and incubated for 15 min in 1% $H_2O_2$ in KPBS to remove endogenous peroxidase activity. Then, sections were rinsed 6 times with KPBS (5 min each) and non-specific binding was blocked in a solution containing 10% NHS, 0.4% Triton X-100, and KPBS at room temperature for 2 h. This was followed by incubation at 4°C for 48 h with mouse anti-GFAP (1:4000; #814369; Boehringer Mannheim) in 1% NHS and 0.4% Triton X-100 in KPBS. Sections were washed with KPBS (3 times 10 min) and incubated for 2 h at room temperature in a secondary antibody solution containing biotinylated horse anti-mouse IgG (1:200; BA-2000; Vector laboratories), 1% NHS, and 0.4% Triton X-100 in KPBS. Sections were washed 3 times with KPBS (10 min each) and moved to 1% avidin-biotin (PK-4000; Vector Laboratories) in KPBS for 1 h at room temperature. After washing, the sections were recycled back to the secondary antibody solution for 45 min, and then to the avidin-biotin solution for 30 min. The secondary antibody was visualized with 0.05% DAB (Pierce Chemical) and 0.04% $H_2O_2$ in KPBS. Finally, sections were washed with 0.1 M PB, and mounted on gelatin-coated microscope slides, and then dried overnight at 37°C. The reaction product was intensified with osmium tetroxide ($OsO_4$; #19170; Electron Microscopy Sciences) and thiocarbohydrazide (#21900; Electron Microscopy Sciences) according to the method of Lewis et al. (1986).

### *3.5. Two-dimensional Fourier analysis*

After *ex vivo* imaging, the myelin- and GFAP-stained sections were utilized for 2D Fourier analysis from control and status epilepticus rats. Three regions of interest were

analyzed including the corpus callosum, cortex and CA3b in the hippocampus. 2D Fourier analysis was done in three consecutive sections from both stainings, myelin and GFAP, for each animal.

Our 2D analysis followed the concept drawn in the previous works (Josso et al., 2005; Marquez, 2006; Budde et al., 2011) with some modifications. The stages of two dimensional analysis, quantitative histology are as follows (the Matlab codes are presented to each relative step by the software-specific font):

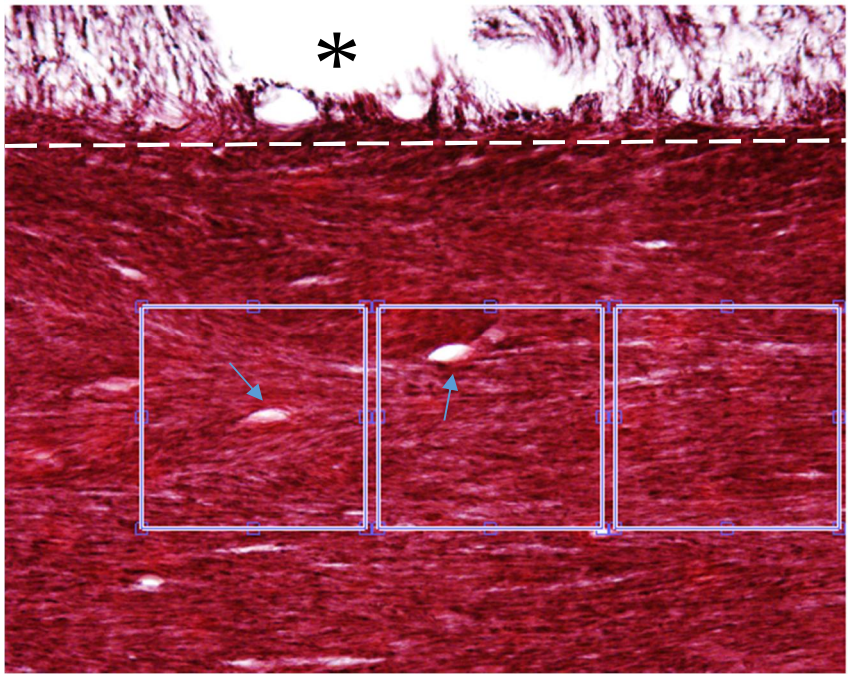


Fig. 4. Representation of the ROI positioning on a myelin-stained section of the corpus callosum of a rat brain. The ROIs were placed continuously and in the same direction from right to left. They were approximately within the same distance from the horizontal reference region (the white dashed line) as well. The axonal orientation is clearly medio-lateral. Vessels are shown by arrows. The region which was used as a vertical reference is marked by the asterisk.

a) A region of interest (ROI) with a square dimension of *1020×1020* pixels was applied to histological sections of control and status epilepticus animals. These dimensions are approximately the same as a DTI voxel. The ROIs were put in place with reference from both vertical and horizontal pin points (Fig. 4). The following shows the Matlab code used for this purpose:

```
ROI{1}.image = double(imadjust(rgb2gray(image)));
```

```
ROI{1}.image = (image-255)*(-1);

clear image

magnitude = (1 - (mean(mean(ROI{1}.image)) / 256)) * 100;

if size(ROI{1}.image, 1) ~= size(ROI{1}.image, 2)
    clear all
    error('Image selected must be square')
end
```

b) In order to minimize the edge-spike effects in Fourier analysis (Ayres et al., 2008), images were filtered (multiplied) by a circular Tukey window with a tapering degree of $\alpha = 0.2$ (Fig. 5), with the center of each image being the reference point.

```
tukey2d =
tukeywin(size(ROI{1}.image,1),.2)*tukeywin(size(ROI{1}.image,2),
.2)';
```

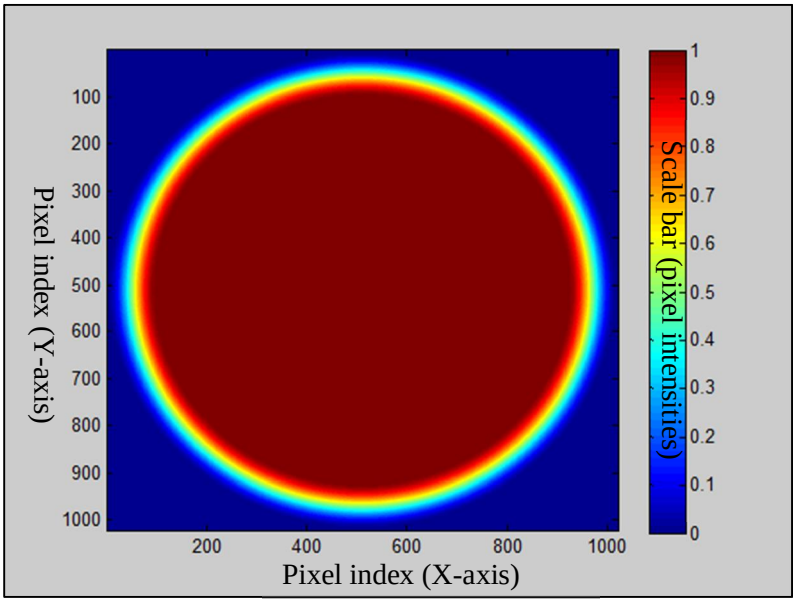


Fig. 5. Visualization of a Tukey window imposed on an indexed image in the spatial domain. The scale bar shows the intensities from 0 (dark blue) to 1 (red-brown). This type of filter excludes the image edges by setting their intensities to 0. Consequently, this filter is expected to eliminate the edge spike effects of the Fourier transformation.

The equation representing the Tukey window ($\omega_0$):

$$\omega_0 = \begin{cases} 1 & r \leq (1-\alpha)N_m \\ \frac{1}{2}\left[1 + \cos\left(\pi\left(\frac{2r-1}{\alpha N} - \frac{1}{\alpha} + 1\right)\right)\right] & (1-\alpha)N_m \leq r \leq N_m \\ 0 & N_m \leq r \end{cases}$$

Where

$$N_m = \frac{N+1}{2}$$

c) Subsequently, a 2D-Fast Fourier Transformation (FFT) was applied to the above mentioned filtered image;

```
ROI{1}.kspace = fftshift(log(abs(fft2(ROI{1}.image.*tukey2d))));
ffted = fftshift(abs(fft2(ROI{1}.image.*tukey2d)));
ffted = ROI{1}.kspace;
```

d) Then the Fourier image was indexed. Assuming the rectangular image has the dimension of $M \times N$ pixels, the distance of each pixel in the image from the center is:

$$r = \sqrt{(X_{cn})^2 + (Y_{cn})^2}$$

Where

$$Y_{cn} = y - \left(\frac{N-1}{2}\right)$$

and

$$X_{cn} = x - \left(\frac{M-1}{2}\right)$$

e) A new function named as NRI was introduced that stands for ‘‘Negative-regions´ Indicator’’. By means of a conditional code, NRI multiplies a minus to the output angle of orientation for negative values of *Y* coordinates based on having the $r_v$. This leads to a unique angle for the pixels situated in negative regions of the image regarding its center, see Fig.6.

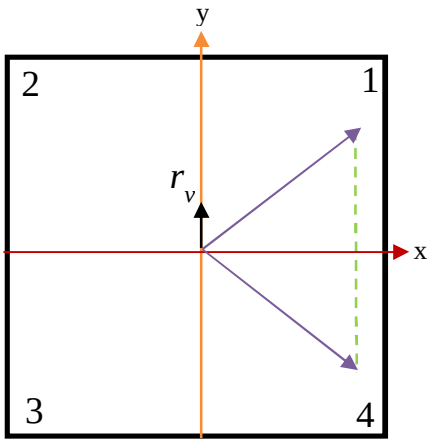


Fig.6. Representation of a square image with four different regions (sub-squares numbered 1-4). The cosine function range is within regions 1 and 2. As a result if the vector representing a pixel sits in regions 3 or 4 (having negative *Y* values), it returns a value mirrored towards the positive *Y*-axis.

As a result, the indexing of the Fourier image is:

```
ii_new = (1:size(ffted,1));
iind_new = ii_new - (size(ffted,1)+1)/2;
iind_all_t = repmat(iind_new,size(ffted,2),1);
iind_all = reshape(iind_all_t,1,[]);
jj_new = (1:size(ffted,2));
jind_new = jj_new - (size(ffted,2)+1)/2;
jind_all = repmat(jind_new,1,size(ffted,1));
NRI_NEW = ones(size(jind_all));
NRI_NEW(jind_all<0) = -1;
iind_all_sq = iind_all.*iind_all;
jind_all_sq = jind_all.*jind_all;
```

f) For the purpose of calculating the angle of orientation, the dot product approach was utilized (Fig. 7). One reference vector ($r_v$) with unit length was introduced sitting on the X-axis of Cartesian coordinate system:

While the other vector represents each indexed pixel in the image.

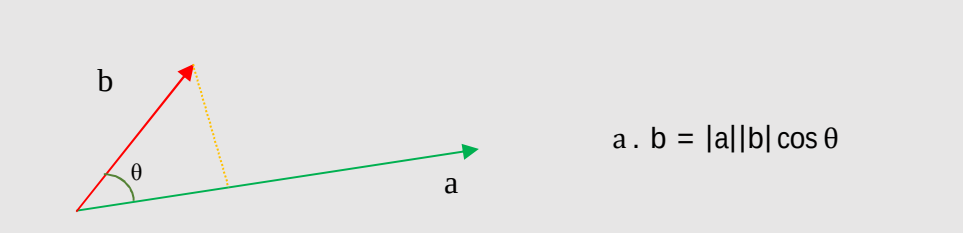


Fig. 7. Illustration of the calculation of the angle between two vectors: a (green) and b (red); one of these vectors is $r_v$ and the other is the vector representing each pixel of the image. The equation in the right side indicates the dot product of two vectors a and b.

g) The angle of orientation was calculated by the inverse cosine function of the dot product of the two vectors divided by the multiplication of their absolute values :

$$\theta = cos^{-1}\left(\frac{a.b}{|a||b|}\right)$$

```
rv = [1;0];
im_vectors = [iind_all;jind_all];
rv_total = repmat(rv,1,size(im_vectors,2));
alfas = NRI_NEW .* acos(dot(im_vectors,rv_total,1)./norms);
```

h) A scatter matrix was formed from Fourier transformed image:

$$X = \begin{bmatrix} A_1 cos\,\theta_1 & \dots & A_n cos\,\theta_n \\ A_1 sin\,\theta_1 & \dots & A_n sin\,\theta_n \end{bmatrix}$$

Where $A_i$ and $\theta_i$ are the pixel intensities and angles respectively;

```
X(1,:)= FFTED .* cos(alfas);
X(2,:)= FFTED .* sin(alfas);
```

i) The covariance matrix formed from $X$:

$$Cov = XX^T$$

j) Matlab´s singular value decomposition syntax applied to matrix *Cov*, that outputs three matrices including the diagonal matrix *S*, in which non-zero arrays are the eigenvalues. Singular value decomposition was then applied to the matrix *Cov*:

$$[U, S, V] = SVD(Cov)$$

where *U* contains the eigenvectors, and

$$S = \begin{bmatrix} \lambda_1 & 0 \\ 0 & \lambda_2 \end{bmatrix}$$

the eigenvalues of the matrix *Cov*.

```
C = X*X';
[U,S,V] = svd(C);
clear C;
lambda(1) = S(1,1);
lambda(2) = S(2,2);
clear tukey2d;
```

k) Anisotropy was calculated by the ratio of the two eigenvectors $\lambda_1$ and $\lambda_2$ which resulted from the singular value decomposition (SVD) of the covariance matrix *Cov* (Fig. 8):

$$AI = 1 - \left(\frac{\lambda_2}{\lambda_1}\right)$$

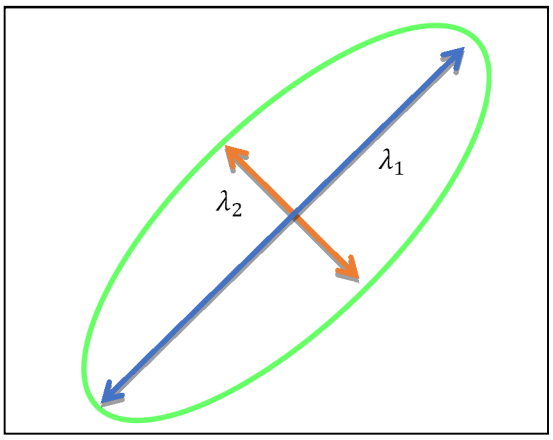


Fig. 8. 2D anisotropy ellipse. An ellipse illustrating the visualization of the fiber orientation built upon two orthogonal eigenvalues $\lambda_1$and $\lambda_2$ resulted from 2D-FT, in order to simulate the diffusion ellipsoid (3D) in 2D. This image represents a highly anisotropic media, such as the coherent fibers of the corpus callosum, where the magnitude of $\lambda_1$ is significantly bigger compared to $\lambda_2$. FT, Fourier transformation, 2D, two dimensional, 3D, three dimensional.

In order to compare the degree of orientation in DTI data, the Cartesian components of diffusion eigenvectors were used to produce a 2D angle relative to 2D-FT´s direction of reference. In other words, *Z* component representing the rostral-caudal dimension had been excluded:

$$\theta = \tan^{-1}\left(\frac{x}{y}\right)$$

Fig. 9 exhibits an example of the ellipse formed in an ROI from crossing fibers in the cortex.

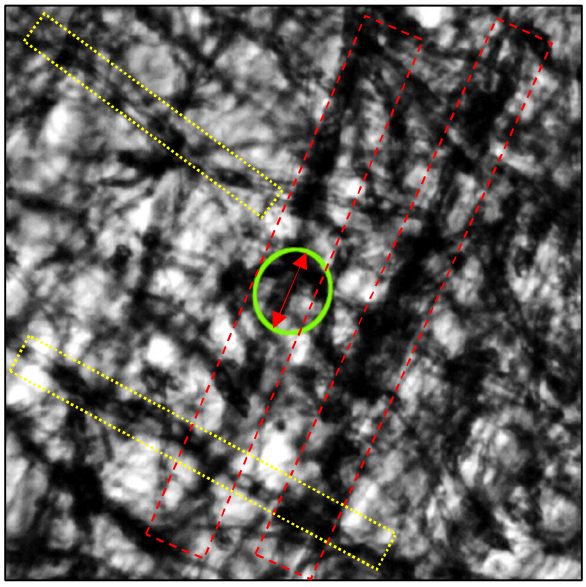

Fig. 9. 2D ellipse in grey matter with crossing fibers. The green ellipse shows visualization of the anisotropy and orientation of the dominant fibers (the red double arrow), by the ellipse in a ROI in the myelin stained cortex. The approximately circular shape of ellipse indicates that the medium is highly isotropic. The dominant fibers with orientation agreeing with the main axis of the ellipse (red double arrow) are marked with red dashed rectangles, to indicate how principle component analysis of 2D-FT calculates the dominant fibers compared to less affective contributors (fiber directionalities with the yellow dashed rectangle) which are crossing the dominant fibers, almost in 90 degrees.

### *3.6. Sample preparation and acquisition for SBEM*

After *ex vivo* MRI, selected brains were sectioned into 1 mm-thick sections, and tissue blocks of the areas of interest were cut into ~1 x 1 x 1 $mm^3$,stained with heavy metals, embedded in resin and trimmed to ~300 x 300 x 500 $\mu m^3$. The trimmed specimen was further mounted on a pin and imaged by means of 3D-EM. Data sets were acquired in a SEM microscope (Quanta

250 Field Emission Gun; FEI, Hillsboro, OR) using a backscattered electron detector with 3View system (Gatan Inc., Pleasanton, CA, USA). Brain samples were imaged with 2 kV beam voltage, spot size 4000, and 1.1e$^{-5}$ Torr pressure. We collected up to 3000 images per data set with a resolution of 50 x 50 x 50 nm$^3$ of a volume at least of 150 x 150 x 200 µm$^3$.

### *3.7. Three dimensional analysis*

The correlation among the regions and volumes of interest for 2D-FT, 3D-FT and DTI analysis is corroborated by Fig. 10. The Spherical coordinate system was used to index the 3D Fourier image due to its simpler concept for detecting the orientation angle. The benefit

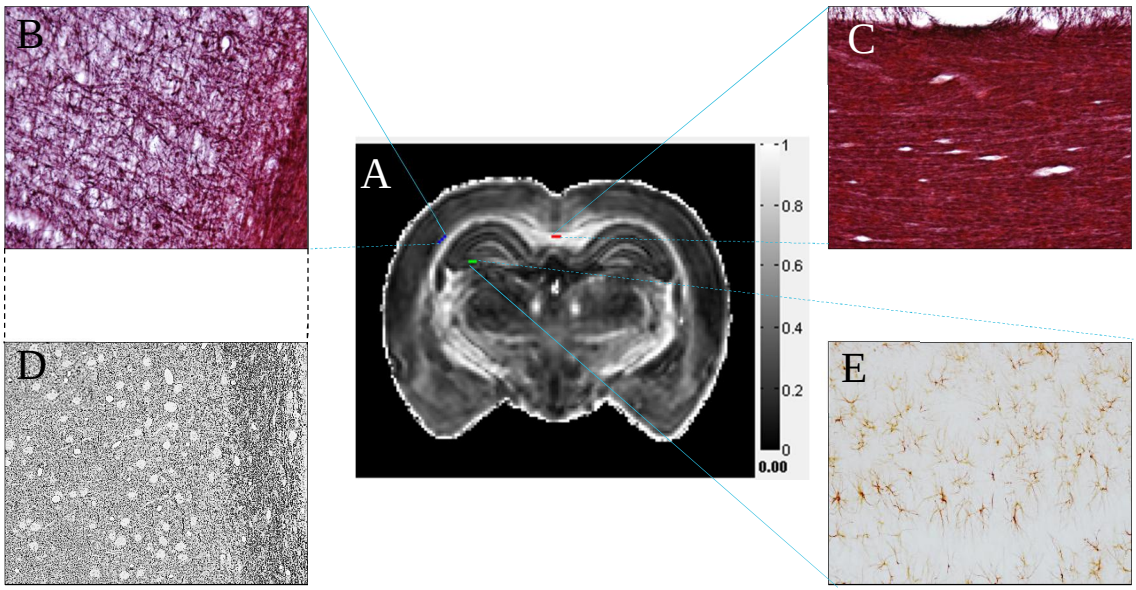


Fig. 10. The precision in correlating DTI-2D-3D analyses. (A) ROI selection in the FA map of the whole brain of the study animal. The grey scale at the right side of the image indicates FA from 0 (isotropic diffusion) to 1 (anisotropic diffusion). Three different ROIs are further extended to their corresponding 2D histology images. Three consecutive voxels are shown for cortex (dark blue), corpus callosum (red) and CA3b (green). (B) Myelin-stained section of the cortex, the extension dashed lines (light-blue) show the corresponding voxels analyzed in DTI (at the center) and the black dashed lines correspond it to the SBEM. Note that the border between grey matter (crossing fibers) and white matter (densely packed fibers) is clearly visible. (C) Myelin-stained section of the corpus callosum, showing the distinct right-left directionality of the axons. (D) SBEM block from the contralateral cortex of a TBI rat. The darker area is the external capsule (white matter) and the lighter grey area is the cortex (grey matter). (E) GFAP-immunostaining section of the CA3b area in the hippocampus.

of using the spherical coordinates instead of the Cartesian system was that each voxel´s position in space (r) can be replaced with the power summation A(annulus).

For a particular point $p(x, y, z)$ being the input to Matlab's syntax for Cartesian to spherical conversion, the output will be three spherical coordinates$(r, \theta, \varphi)$. In appendix 1 we provided an explanation for the compliance between conventional and Matlab elevation angles. The tissues processed for SBEM from normal and injured rat brain was used as a model for TBI. A volume of interest (VOI) was introduced to the SBEM block with dimensions approximately consistent to the resolution of 2D-ROIs.

The Matlab code written in the vectorized form was further optimized and hence, made faster and more efficient. The spherical coordinate system had similarly been used for characterization of anisotropy in diffusion weighted MRI (Frank, 2002).

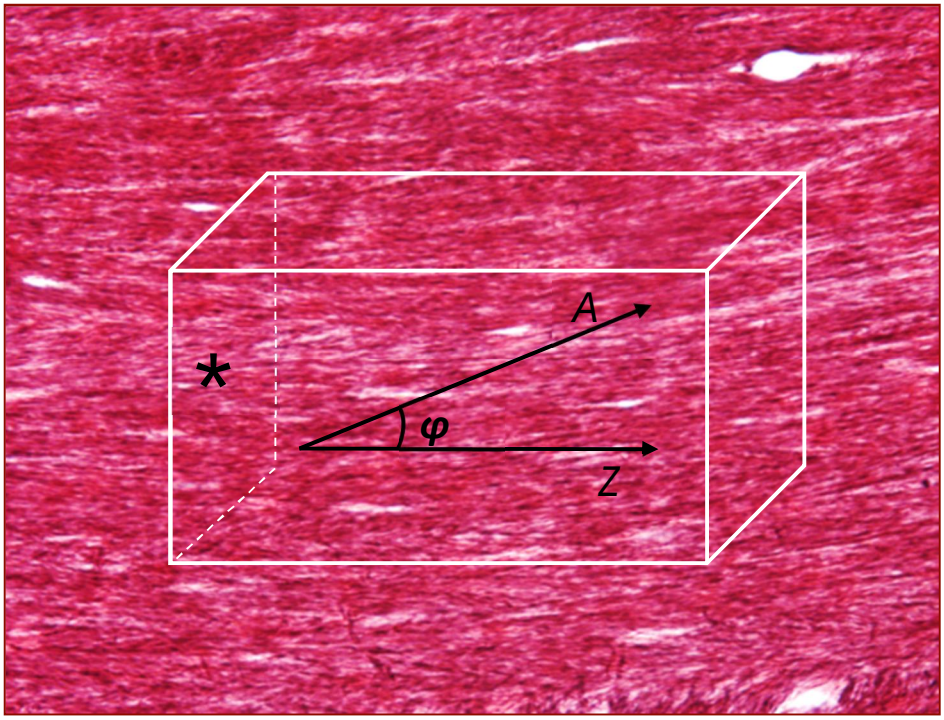


Fig. 11. 2D and 3D compatibility based on the directionality of the myelinated axons. This is a schematic exhibition for the directional similarity of the SBEM block (white rectangular cube) with the myelin-stained image of the corpus callosum (background). The *Z* and *A* arrows respectively indicate the primary (dominant directionality) dimension of the SBEM block and the overall direction of the axons (whether in 2D histology or in 3D) calculated by principal component analysis of Fourier transformation. In conclusion, $\varphi$ was the elevation angle between these two vectors calculated with regard to a reference plane (marked by the asterisk). Thus, $\varphi$ was expected to be the same angle drawn from 2DFT.

The stages of 3D-FT analysis are as follows:

a) A VOI was chosen by first defining (x, y, z) of the corner point as its reference point (Fig.11). Subsequently, a fixed length to that point was added for building a cubic voxel from that point of reference. The point picking was done by the help of ImageJ visualization. For the corpus callosum for example, the image stack was investigate to avoid placing the VOIs on the stack groups which contained distortions or edge defects. For the cortex, it was tried to carefully inspect the block to avoid overlapping of the VOIs and also to properly choose VOI coordinates in the cortex and external capsule. A difference in the definition of the image in Matlab versus ImageJ was noticed in the way that x and y coordinate of a point were assigned differently in either software. This is obvious from the Matlab´s vertical and horizontal indexing system of axes of Fig.5.

b) A ball-like Tukey filter was applied to each VOI for conquering the edge spike effects, similar to the circular Tukey filter used for 2D-FT analysis. To put it simply, instead of a circle it had to be a volume Tukey in shape of a sphere:

```
function tukey3d = tukey3D(Xdim,Ydim,Zdim,alfa)
ii = (1:Xdim);
jj = (1:Ydim);
kk = (1:Zdim);
cub2 = Xdim*Ydim;
Icn = ii-(Xdim+1)/2;
Jcn = jj-(Ydim+1)/2;
Kcn = kk-(Zdim+1)/2;
Jind = repmat(Jcn,Ydim,1);
Jind_v = reshape(Jind,1,[]);
jind_al= repmat(Jind_v,1,Zdim);
iind_al = repmat(Icn,1,Zdim*Ydim);
kk_ny = repmat(Kcn,cub2,1);
kind_al = reshape(kk_ny,1,[]);
Nm = Xdim;
r = sqrt((iind_al.*iind_al)+ (jind_al.*jind_al)+
(kind_al.*kind_al));
alfa = 0.2;
hfsiz = (Nm+1)/2;
omega = 0.5*(1+cos(pi*((2*r-1)/(alfa*Nm)-(1/alfa)+1)));
omega (r < ((1-alfa)*hfsiz)) = 1;
omega(hfsiz <= r) =0;
tukey3d = reshape(omega,Xdim,Ydim,Zdim);
Ydim = size(B,2);
Xdim = size(B,1);
Zdim = size(B,3);
```

```
alfa = 0.2;
tukey3d = tukey3D(Xdim,Ydim,Zdim,alfa);
img = B.*tukey3d;
```

c) The real part of the filtered image (absolute values) was then 3D Fourier transformed, by applying the multidimensional (n-dimensional) fast Fourier transform:

```
fftd = fftshift((abs(fftn(img))));
```

d) Then, the $3 \times N$ scatter matrix was founded in the Cartesian form, while rephrased in the spherical format:

$$X = \begin{bmatrix} A_1 \cos\varphi_1 \cos\theta_1 & \dots & A_n \cos\varphi_n \cos\theta_n \\ A_1 \cos\varphi_1 \sin\theta_1 & \dots & A_n \cos\varphi_n \sin\theta_n \\ A_1 \sin\varphi_1 & \dots & A_n \sin\varphi_n \end{bmatrix}$$

The first, second and third rows of the above matrix respectively represented $x$, $y$ and $z$ values for all the voxels indexed inside the VOI. In order to get directionality, each voxel´s distance was replaced with Fourier intensities ($A_1 \dots A_n$):

```
[az,el,removevecs] = cart2sph(x,y,z);
maxdist = 100;
mindist = 11;
removevecs(removevecs>maxdist) = 0;
removevecs(removevecs<mindist) = 0;
removevecs(removevecs>=mindist) = 1;
el(removevecs==0) = [];
az(removevecs==0) = [];
fftd(removevecs==0)=[];
X(1,:) = fftd.*cos(el).*cos(az);
X(2,:) = fftd.*cos(el).*sin(az);
X(3,:) = fftd.*sin(el);
clear x y z
clear removevecs el az
```

e) Then similarly to 2D analysis, the covariance matrix *C* was formed by multiplying the scatter matrix by its transpose:

$$C = XX^T$$

f) The Matlab syntax used for applying the singular value decomposition to the covariance matrix, so as to produce three eigenvalues:

$$[U, S, V] = SVD(C)$$

Where *U* contained the eigenvectors, and *S* the eigenvalues of the matrix *C*.

Finally, three eigenvectors constitute the three diameters of the ellipsoid, $\lambda_1$ being the largest diameter, $\lambda_2$being the medium and $\lambda_3$ the smallest one, perpendicularly to one another (Fig. 12). Since 3D-FT measures the density of membranes that restrict the water diffusion, the minor eigenvalue reflects the least hindered orientation. This means that $\lambda_3$ from 3D-FT corresponds to the diffusion tensor orientation:

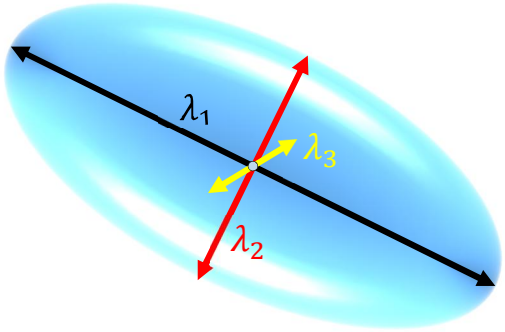


Fig. 12. Visualization of the ellipsoid indicating the directionality, formed upon the three eigenvalues in three orthogonal directions. This figure is presumably representing an anisotropic directionality, a characteristic of the coherent fiber structures as in the white matter. The dominance of $\lambda_1$ over the other two eigenvectors is clearly visible, a phenomenon observed in diffusion tensor of the water molecules in the corpus callosum.

Anisotropy was calculated upon the three eigenvalues (Basser and Pajevic, 2000):

$$AI = \sqrt{\frac{(\lambda_1 - \lambda_2)^2 + (\lambda_2 - \lambda_3)^2 + (\lambda_1 - \lambda_3)^2}{2(\lambda_1 + \lambda_2 + \lambda_3)^2}}$$

If the three eigenvalues did not vary from one another it would result in a more isotropic directionality. The elevation angle ($\varphi$) for the primary direction represented the tilted angle of the fiber bundles throughout the main direction of image stacks (see Fig. 11).

```
C = X*X';
```

```
[U,S,V] = svd(C);
[azu11,elu11,ru11] = cart2sph(U(1,1),U(1,2),U(1,3));
[azu12,elu12,ru12] = cart2sph(U(2,1),U(2,2),U(2,3));
[azu13,elu13,ru13] = cart2sph(U(3,1),U(3,2),U(3,3));

angl(1,:)=[azu11 elu11];
angl(2,:)=[azu12 elu12];
angl(3,:)=[azu13 elu13];
ld(1) = S(1,1);
ld(2) = S(2,2);
ld(3) = S(3,3);
p = ld(:,1);
q = ld(:,2);
d = ld(:,3);

AI= sqrt(((p-q)*(p-q)+(p-d)*(p-d)+(q-d)*(q-d))/(2*(p*p)+(q*q)+(d*d)));
```

## 4. STATISTICAL ANALYSIS

The comparison between groups was conducted using Mann Whitney T-test. Values are represented as mean ± standard error of the means. Graphs were drawn by using Graph Pad Prism (version 5.03).

# 5. RESULTS

## *5.1. DTI and 2D-Fourier analysis of control and status epilepticus rats*

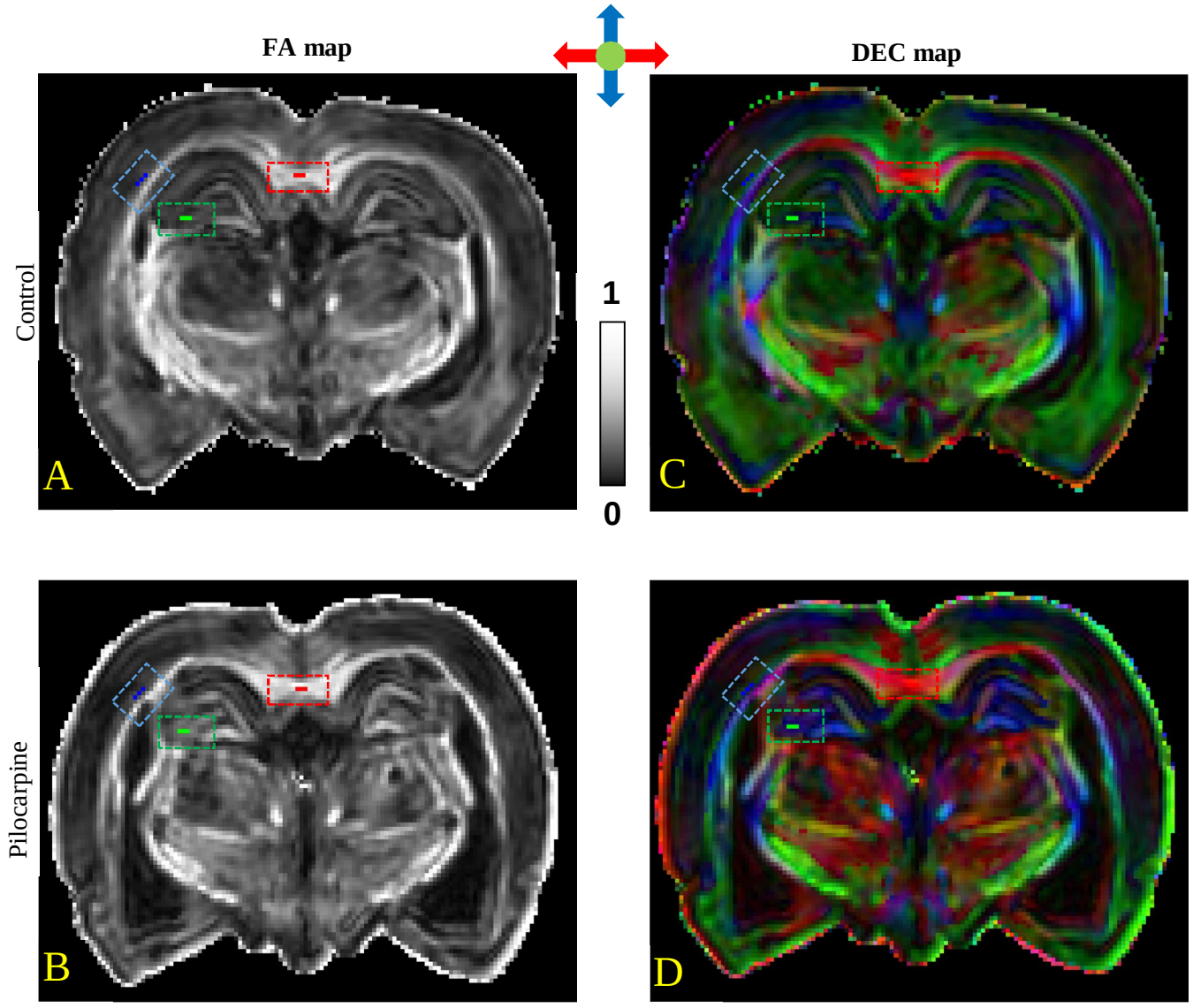


Fig. 13. Regions of interests (ROI) in the FA maps (A, B) and directionally encoded colormap (DEC) maps (C, D) of control (A, C) and status epilepticus (B, D) rats. The dashed rectangles indicate the area of the corpus callosum (red), CA3b of the hippocampus (green) and the cortex (blue) where the ROI is located (solid lines). FA maps: grey scale bar indicates the anisotropy ranging from 0 (black) up to 1(white); DEC colors: *red* medial-lateral, *green* rostral-caudal and *blue* dorsal–ventral.

Fig. 13 shows the location of the ROIs in DTI maps for control and status epilepticus brains in corpus callosum, CA3b and cortex. For each of these three different areas of the brain,

three voxels were manually picked and averaged. We analyzed the same locations in myelin and GFAP stained sections using 2D-FT.

### 5.1.1. Corpus callosum

The corpus callosum showed slightly brighter voxels in status epilepticus animals (Fig. 13B) as compared to controls (Fig. 13A), indicating that FA might be increased in the corpus callosum of pilocarpine animals.

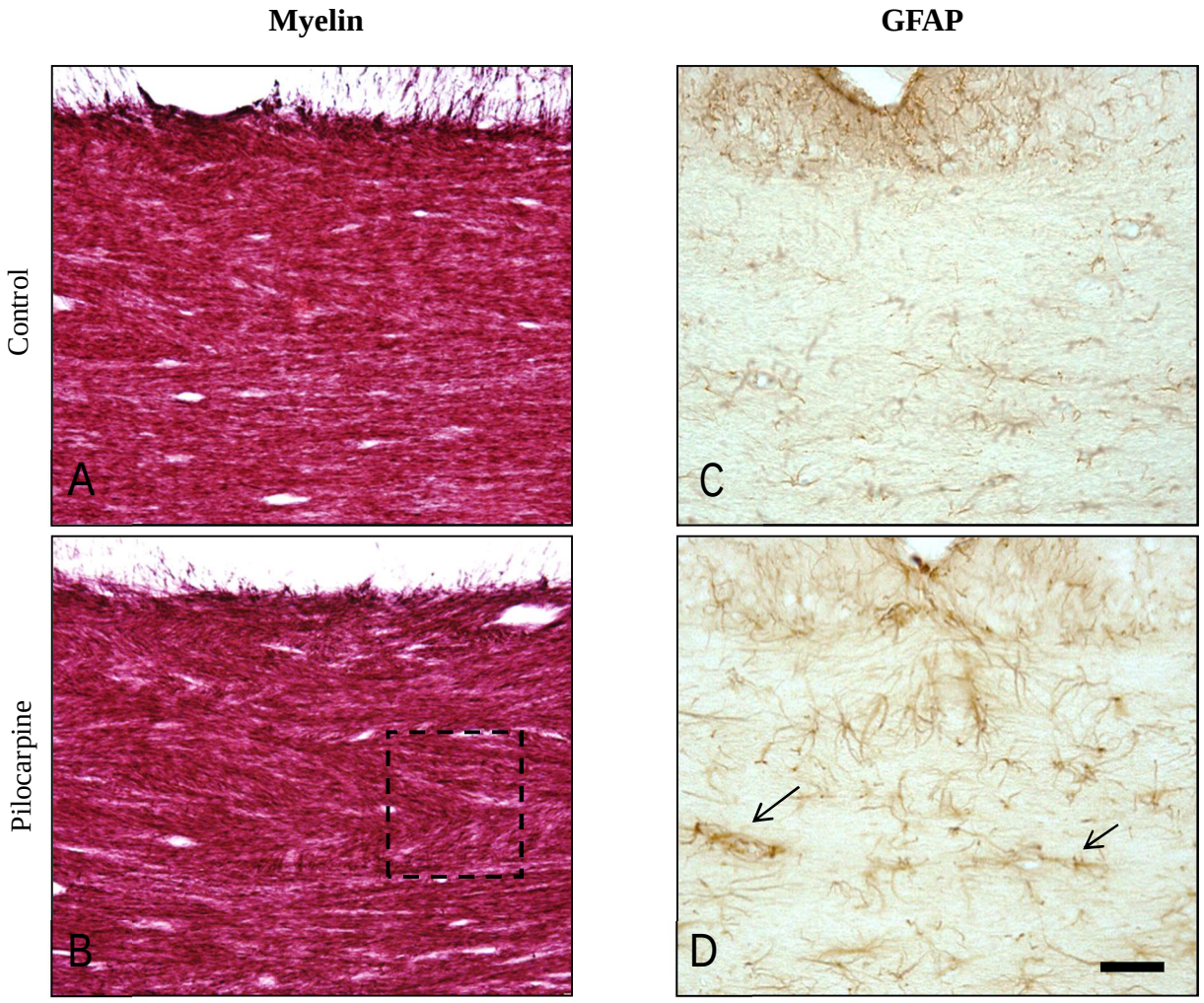


Fig. 14. Myelin (A, B) and GFAP (C, D) histological stainings of the corpus callosum of a control (A, C) and a pilocarpine treated rat (B, D). This picture illustrates the microstructural changes which occur after status epilepticus related to the myelinated axons and astrocytes. The dashed rectangle in B shows altering directionalities of the myelinated axons. Arrows in panel D indicate the activate astrocytes in the corpus callosum of a pilocarpine treated animal. GFAP, glial fibrillary acidic protein. Scale bar: 50 μm.

As it is shown in the above figure, histology revealed a slight change in the directionality of both myelinated axons (Fig. 14B) and astrocytes (Fig. 14D) after status epilepticus as compared to controls (Fig. 14A and 14C).

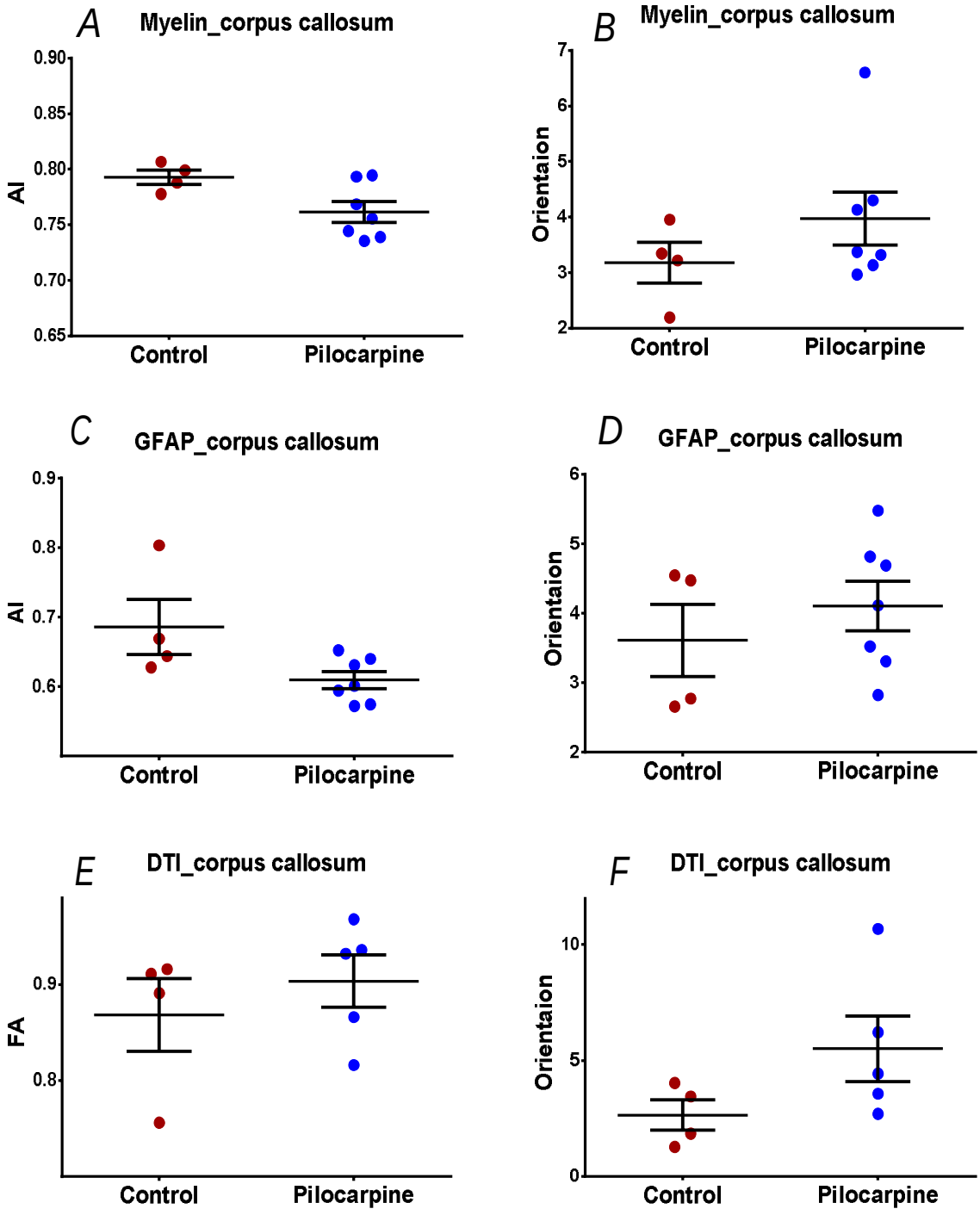


Fig. 15. Results for 2D-FT (A-D) and DTI (E, F) analyses of the corpus callosum. In graphs E,F each dot is an average of three voxels in the ROIs. AI, anisotropy index; FA, fractional anisotropy; GFAP, glial fibrillary acidic protein.

The myelinated axons in the corpus callosum from control brains appeared to be mainly parallel (Fig. 14A) whereas axons in the same area in animals after status epilepticus showed slightly different orientations (Fig. 14B). No difference in myelinated axonal density was observed in animals treated with pilocarpine when compared to controls. GFAP staining showed a distinct growth of astrocytes after status epilepticus with more extended processes in comparison to controls (Fig. 14D). This was a sign of activated astrocytes in this area. It was clearly visible that astrocyte morphologies in the corpus callosum were mostly horizontally-oriented in controls. Albeit the activated astrocytes in status epilepticus animals followed the same pattern, they exhibited numerous processes with a more random orientation (Fig. 14D).

Although we observed these changes in the DTI maps and histological preparations, our values from status epilepticus brains in the corpus callosum did not differ from those in control brains neither in anisotropy nor orientation (Fig. 15). Nevertheless, we observed some trends in the average values obtained from DTI and 2D-FT. 2D-FT showed a trend of declined anisotropy for status epilepticus rats for both stainings (Fig. 15A and 15C). This is in contrast to DTI showing a trend of elevated FA values in animals after pilocarpine treatment than controls (Fig. 15E). The degree of orientation in the corpus callosum showed a trend of increase after status epilepticus in both DTI and 2D-FT (Fig. 15B, 15D and 15F).

Finally, it is worth to mention that the values obtained from DTI were at the same order of magnitude than the values obtained from 2D-FT analysis (Fig. 15). However, anisotropy values obtained from 2D-FT in both stainings (Fig. 15A and 15C) were lower than DTI (Fig. 15E).

### 5.1.2. CA3b in the hippocampus

Fig. 16 shows myelin and GFAP stained sections of the CA3b area in the hippocampus of a control and a status epilepticus rat. In this area, the myelinated axons changed their orientation in a more organized pattern (Fig. 16B) as compared to controls (Fig. 16A). Similarly, the processes of activated astrocytes were more oriented in status epilepticus rats (Fig. 16D) than in controls (Fig. 16C). In some cases, the processes of axons and astrocytes were in perpendicular orientation, as related to the pyramidal cell layer (lower dash line in Fig. 16).

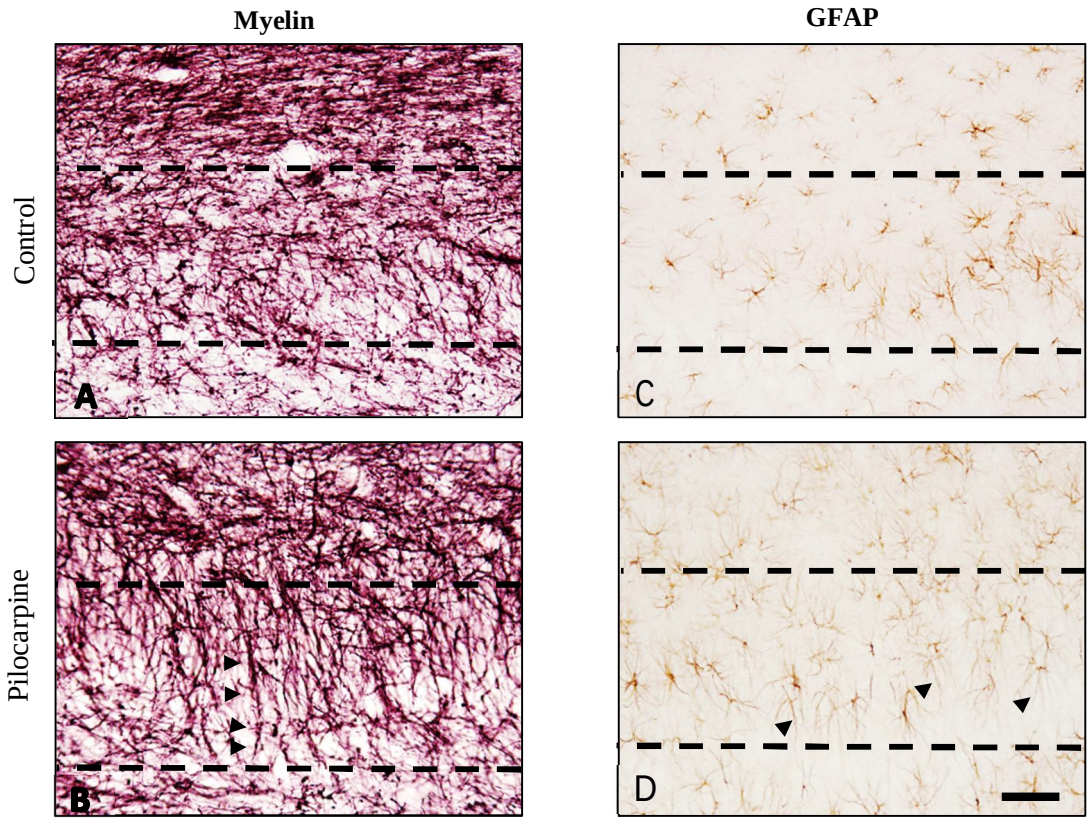


Fig. 16. Organization of fibers in grey matter, hippocampus. Myelin (A, B) and GFAP (C, D) stainings for the CA3b of a control (A,C) and a pilocarpine (B,D) rat. A significant increase in the directionality of axons in the pilocarpine rat is visible (black triangles in panel B). Triangles in panel D indicate the extended processes of the reactive astrocytes in the CA3b of pilocarpine rats which appeared to be more oriented than controls. The dashed line shows the extent of the ROI selection in CA3b. Scale bar: 50 µm. GFAP, glial fibrillary acidic protein

Changes in anisotropy and orientation were found in both stainings by 2D-FT (Fig. 17). Myelinated axons exhibited a significant increase in anisotropy (*$p < 0.05$) (Fig. 17A) and orientation (**$p < 0.01$) (Fig. 17B) after status epilepticus as compared to controls. Likewise, astrocyte processes exhibited a dramatic rise in anisotropy (**$p < 0.01$) (Fig. 17C) and orientation (**$p < 0.01$) (Fig. 17D). DTI analysis in CA3b did not lead to a major change between controls and status epilepticus animals neither for FA (Fig. 17E) nor orientation (Fig. 17F). We also found that FA and orientation values calculated in DTI maps were more dispersed than in 2D-FT. This might be attributed to the difficulty to manually pick a voxel in the CA3b region.

Similar to corpus callosum, the values obtained from 2D-FT were in the same order of magnitude with DTI. Only the orientation values acquired from GFAP-stained sections were higher than DTI, albeit those from myelin stained sections were closer to it.

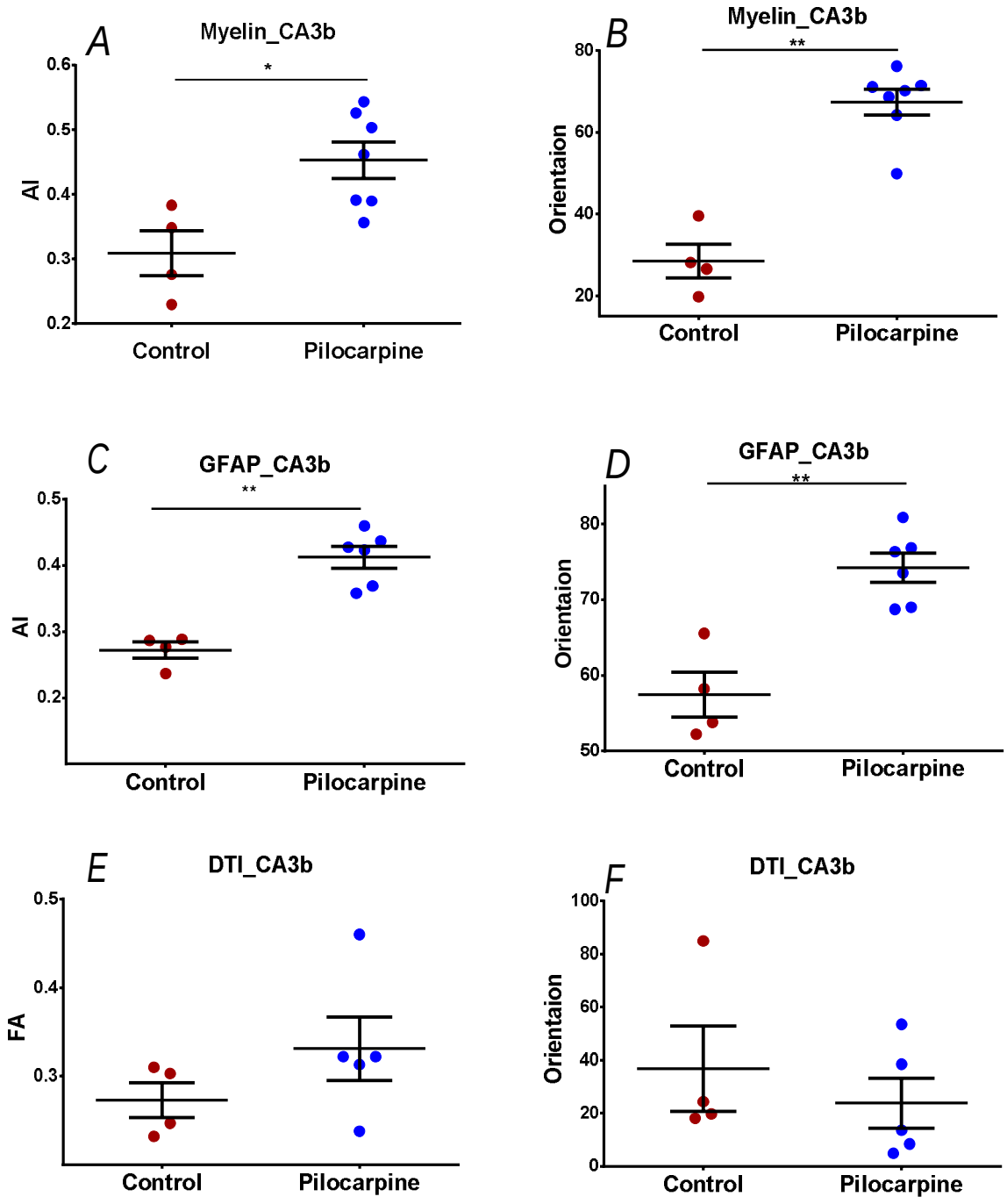


Fig. 17. Result for 2DFT (A-D) and DTI (E, F) analysis of the corpus callosum. In graphs E,F each dot is an average of three voxels in the ROIs. AI, anisotropy index; FA, fractional anisotropy; GFAP, glial fibrillary acidic protein. $* p < 0.05$ and $** p < 0.01$.

### 5.1.3. Cortex

We found diminished microstructural organization for both myelinated axons and astrocytic processes in cortical layer VI among animals after status epilepticus (Fig. 18). Myelinated axons from the external capsule appeared more coherently oriented in controls (Fig. 18A) than in pilocarpine rats (Fig. 18B). Slightly less density of myelinated axons was also observed among these areas in animals after pilocarpine treatment (Fig. 18B). Processes of activated astrocytes were randomly oriented and also the presence of these cells was more pronounced (Fig. 18D).

Similar to the corpus callosum, our DTI and 2D-FT values from status epilepticus brains in the cortex did not differ prominently from those in control brains neither in anisotropy or orientation (Fig. 19).

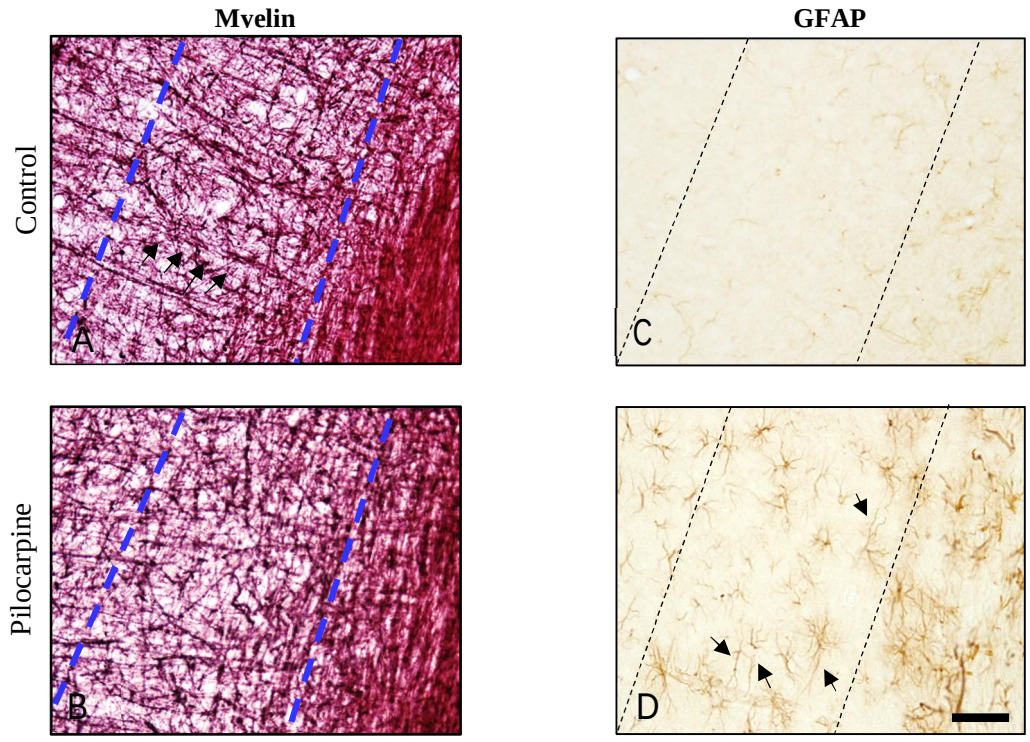


Fig. 18. Organization of fibers in grey matter, layer VI in the cortex. Myelin (A, B) and GFAP (C, D) of the. Arrows in panel A show the distinct pattern of axons in controls. Arrows in panel D also show the prolonged processes of astrocytes that are presumably responsible for increased anisotropy. The dashed lines show the area selected for analysis. Scale bar: 50 µm. GFAP, glial fibrillary acidic protein

We observed some trends in the average values obtained from DTI and 2D-FT. Our histological findings could explain the trend to the decrease of anisotropy values in status epilepticus animals amongst the myelin stained sections (Fig. 19A). The regrowth of reactive astrocytes might justify a slight increase in the anisotropy (Fig. 19C) and orientation angle (Fig. 19D). After status epilepticus, FA showed a trend to increase that seemed rather to be along with the activated astrocytes in the cortex, than the findings in myelin. As though in

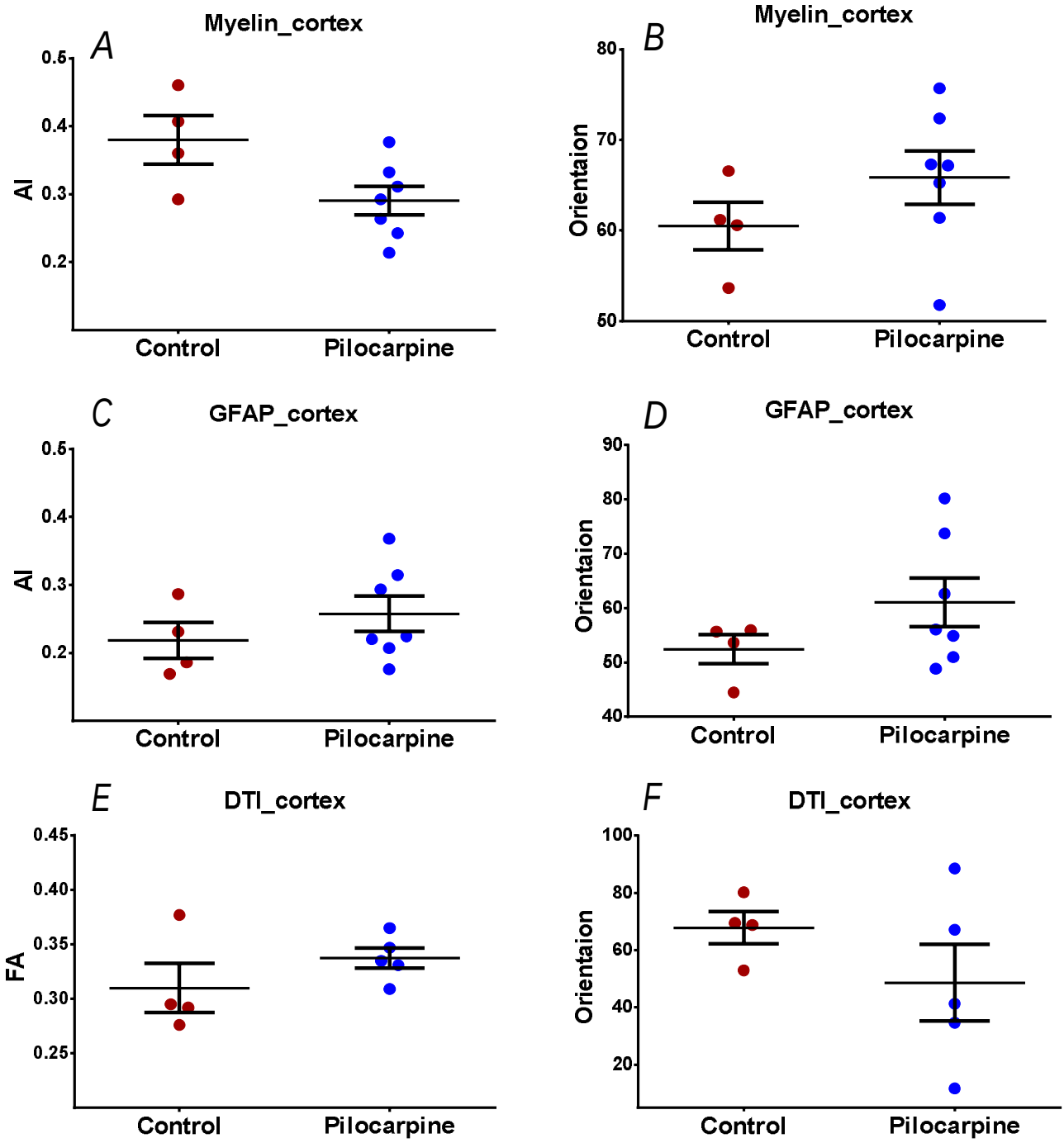


Fig. 19. Result for 2DFT (A-D) and DTI (E, F) analysis of the cortex. In graphs E,F each dot is an average of three voxels in the ROIs. AI, anisotropy index; FA, fractional anisotropy; GFAP, glial fibrillary acidic protein.

CA3b, the difficulty to manually select a voxel in the cortical region might be the reason for the differences in the results in DTI parameters (Fig. 19E and 19F).

### *5.2. Three-Dimensional Fourier Analysis of Electron Microscopy*

#### 5.2.1. Corpus callosum of a naïve rat

Fig. 20 illustrates the 3D block of the corpus callosum of a naïve (control) rat. Fig. 21 shows anisotropy values for larger VOI (0.86 ± 0.01) (Fig. 21C) and smaller VOI had anisotropy value of (0.83 ± 0.007) (Fig. 21A) which were close to that in DTI (0.87 ± 0.04). The small difference between the larger VOI and the smaller VOI might come from the contribution of vessels and cell bodies.

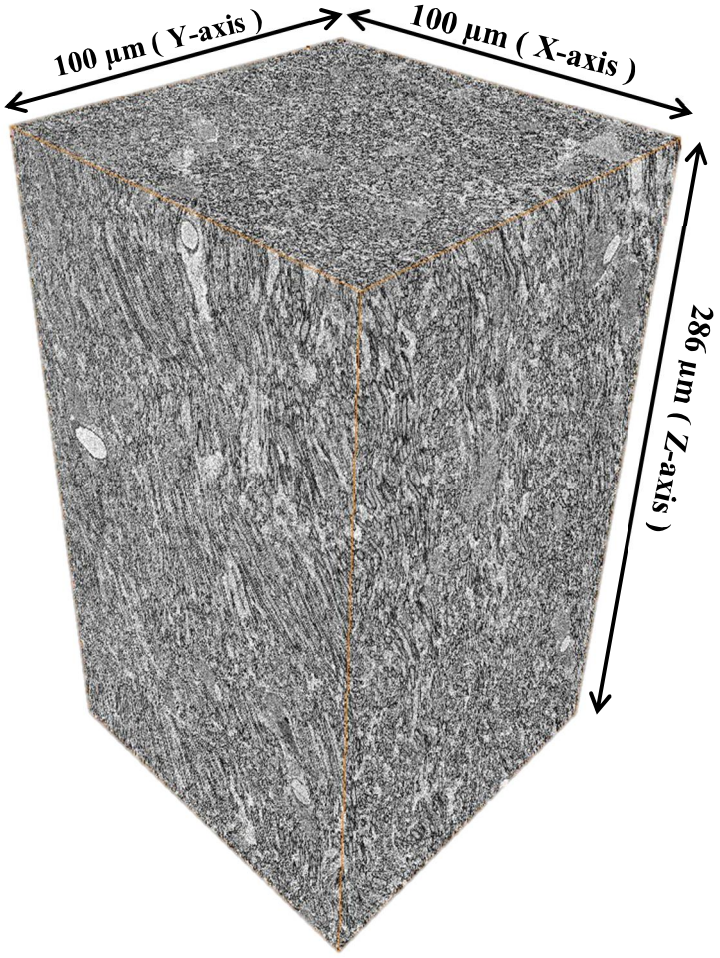


Fig.20. SBEM block of the corpus callosum of a naïve rat in 3D view.

Magnification: 250x, Voltage: 2.1 keV, Resolution: 0.05 x 0.05 x 0.05 $\mu m^3$, pressure (Torr): $1.13e^{-005}$ ,1021 slices. The myelinated axons of the corpus callosum are roughly along Z axis.

Regarding the differences between 2D-FT and 3D-FT values, we could compare those two methods in the corpus callosum of controls in conventional histological preparations and in the naïve animal used in SBEM. The anisotropy of control rats for myelin resulted from 2D-FT was slightly lower than 3D-FT, explaining how the absence of bundles in the third

dimension may affect the results. The fiber orientation in the larger VOIs (77.3 ± 0.7) (Fig. 21D) varied in comparison with the smaller VOIs (68.56 ± 1.6) (Fig. 21B). Again, the difference between the larger VOI and the smaller VOI might come from the contribution other tissue components, such as vessels and cell bodies in affecting the anisotropy.

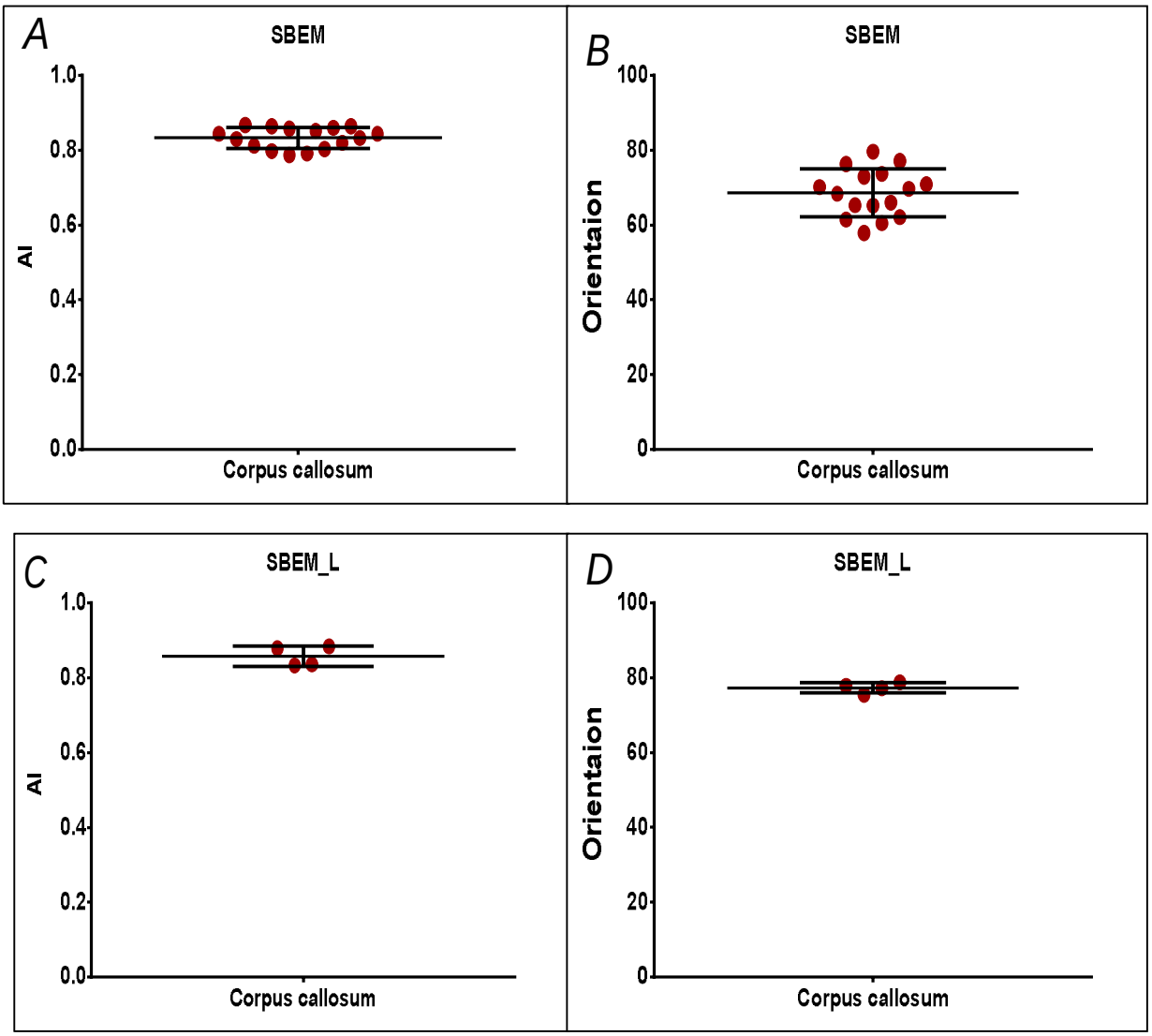


Fig. 21. Results of 3D-Fourier analysis for a naïve rat in the corpus callosum. Each red dot represent one VOI cube that is square (isotropic) in A,B but rectangular (non-isotrpic) in C,D. DTI: diffusion tensor imaging, AI: anisotropy_3D, SBEM: serial block-face electron microscopy, SBEM_L results from large VOI.

Prior to this stage our presumption was that the angle which would be our result must have been the elevation from the reference plane i.e. X-Y which amount around 90°. In order to verify the compatibility of 3D-FT orientation in the corpus callosum with 2D-FT, the fiber

organization was inspected by visualization of the block from other dimensions. Fig. 22 and 23 show the re-slicing function of the same block in Fig. 20 but with 90° rotation. The fiber bundles were inspected through the Y-Z plane, a negligible number of them were found in the opposite directionality with respect to the others as marked with dashed rectangles (Fig. 23).

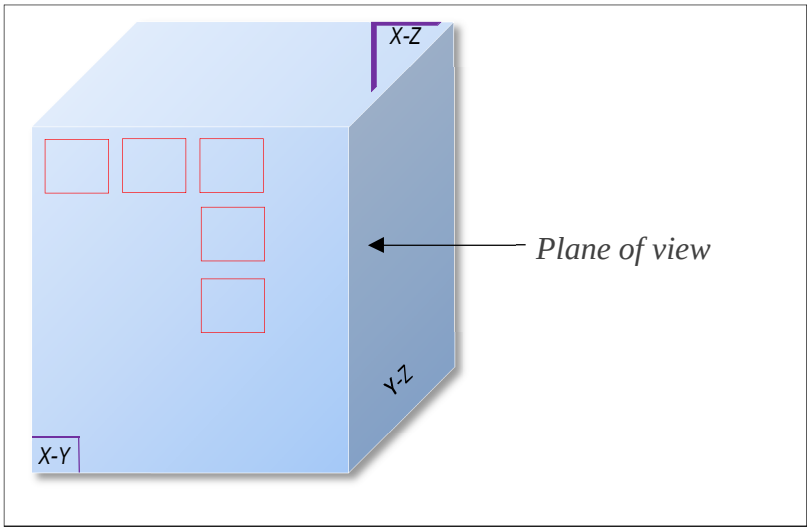


Fig. 22. Schematic SBEM-block and the location of five VOIs (red squares) with varying angles through it. The arrow shows the field of view which was used to detect altering fiber orientations.

Concerning 2D and 3D-FT angles we can observe a variance between the mean degree of myelinated axons for controls hovering around 3° (Fig. 15 B) while for SBEM it is around 70° (Fig. 21 D). Nevertheless, by visually investigating the angle of axons through slices 1 to 500 it can be verified that 70° is true regarding the default reference plane in the SBEM block. The way tissue was cut is absolutely the reason for the majority of fiber bundles not to be parallel to the length of the block, as shown previously in Fig. 11.

In the graphs presented in Fig. 15, 17, and 19, the variability of the angular values was high as compared to anisotropy values. This is evidence for the unreliability of 2D methods to resolve certain orientations. The orientation degree derived from ignoring the third dimension of the DTI for controls is almost 3º which is above the 77° of the SBEM. However it may not be a fair comparison because numerous structures have been taken into account for 2D-DTI angle. Also, it is worth notice that when we prepared the tissue samples for SBEM, the cutting of the tissue might not be perfectly aligned with the DTI maps. The registration of

the SBEM and DTI was not included in this work, and it needs to be included in future studies in order to correct the possible deviations between these two techniques.

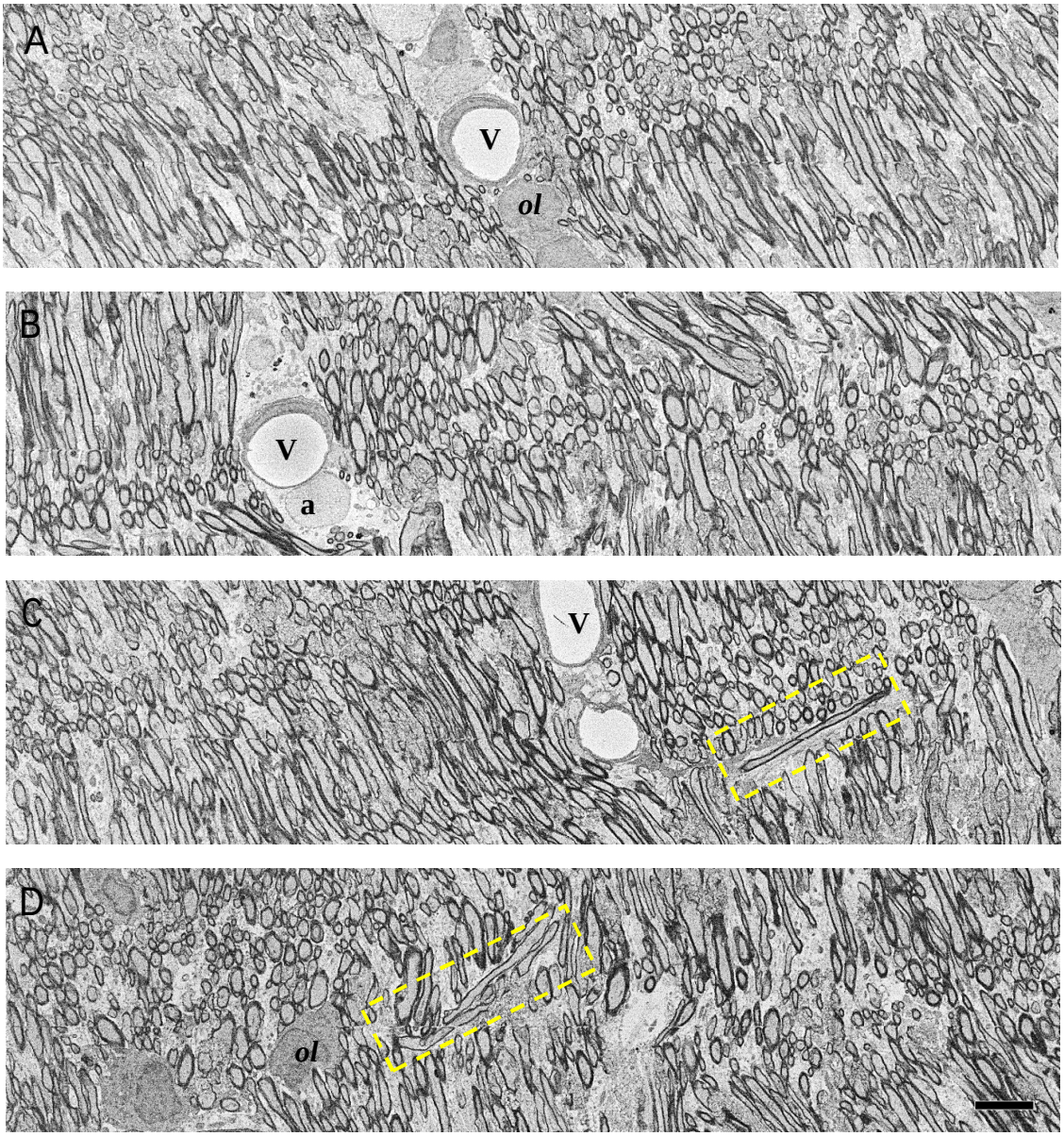


Fig. 23. Four different images from the SBEM-block of the corpus callosum. Panels C and D have axons in perpendicular direction to other ones, as indicated by the yellow dashed rectangles. Abbreviations: a, astrocyte; ol, oligodendrocyte; V, vessel. Scale bar = 6.25 µm.

### 5.2.2. Cortex of a rat after TBI

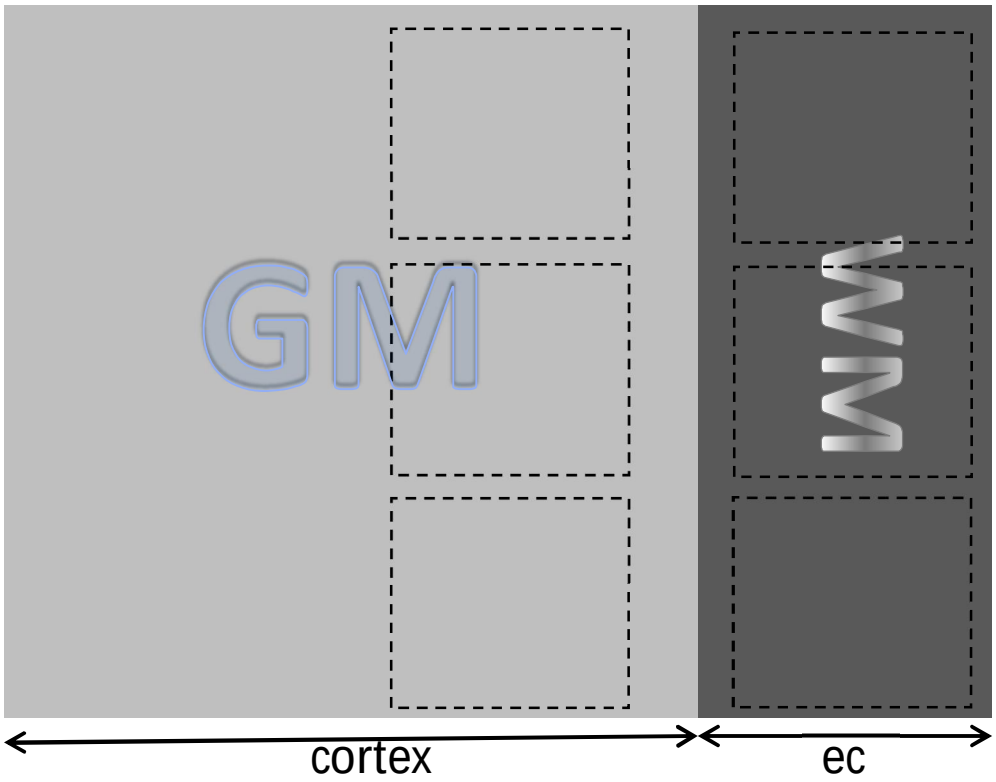


Fig. 24. Location of the VOIs on the *X*-*Y* plane of the SBEM blocks. Three VOIs on the grey matter and three in the white matter were chosen. All VOIs had the same 3D-dimensions. This placement of VOIs is in line with the approach of ROIs in 2DFT. ec, external capsule, GM, grey matter, WM, white matter.

The figure above shows a schematic view of the location of the VOIs in the cortex and external capsule. The analysis involved three VOIs on the cortex and three on the external capsule, all with the same dimensions 200×200×200 voxels (Fig. 24). In Fig. 25, it is shown the location of the VOIs in the DTI maps in the cortex and external capsule.

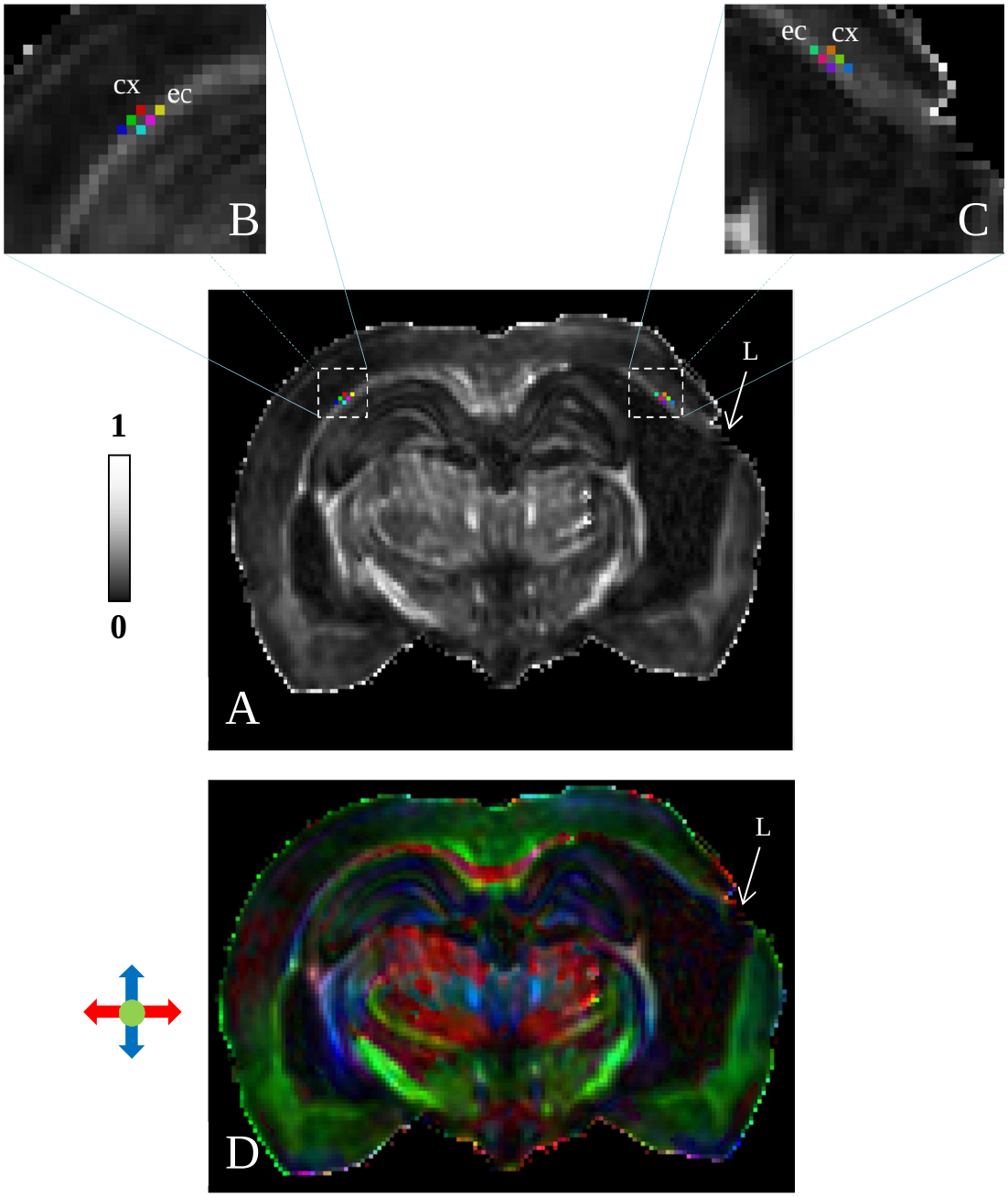


Fig. 25.DTI analysis for trauma rats. Each square element of these images are 3D-voxels (as pixels in 2D images). The 0 to 1 scale bar in the left, indicates FA range by intensity, meaning the higher (brighter) the voxel intensity is, the more anisotropic the dominant fiber directionality will be. A) FA map: the lesion site is marked with an arrow. B) Contralateral VOIs including three voxels in the external capsule and three voxels in the cortex. C) Ipsilateral VOIs in the vicinity of the lesion. D) Directionally encoded color map of the same animal, showing the dominant fiber orientations by the specified colors in each voxel. Color coding: *red* medial- lateral, *green* rostral-caudal and *blue* dorsal-ventral. Abbreviations: cx, cortex; ec, external capsule; L, lesion.

We observed differences in the morphology of the cellular structures in the 3D stacks of SBEM images of the contralateral (Fig. 26A) and ipsilateral cortex (Fig. 26B). For the contralateral cortex, morphology of the neurons, axons and glial cells appeared normal. Particularly, in the external capsule, it could be seen that axons were organized and the myelin sheath was normal. Dendrites and axons in the cortex run perpendicularly to the external capsule into the deep layers of the cortex throughout more superficial ones as normally have been shown in healthy brain. In contrast, the ipsilateral block shows many consequences of the injury.

**26A**

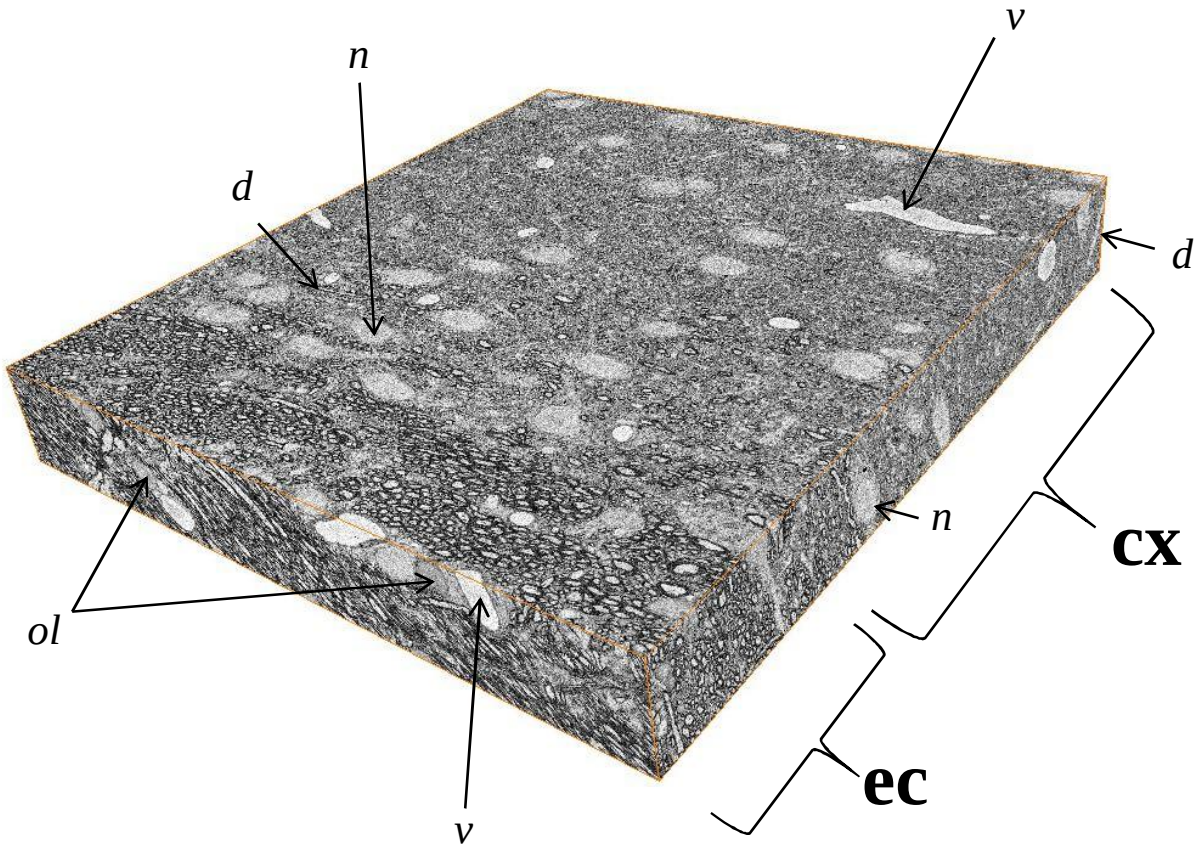

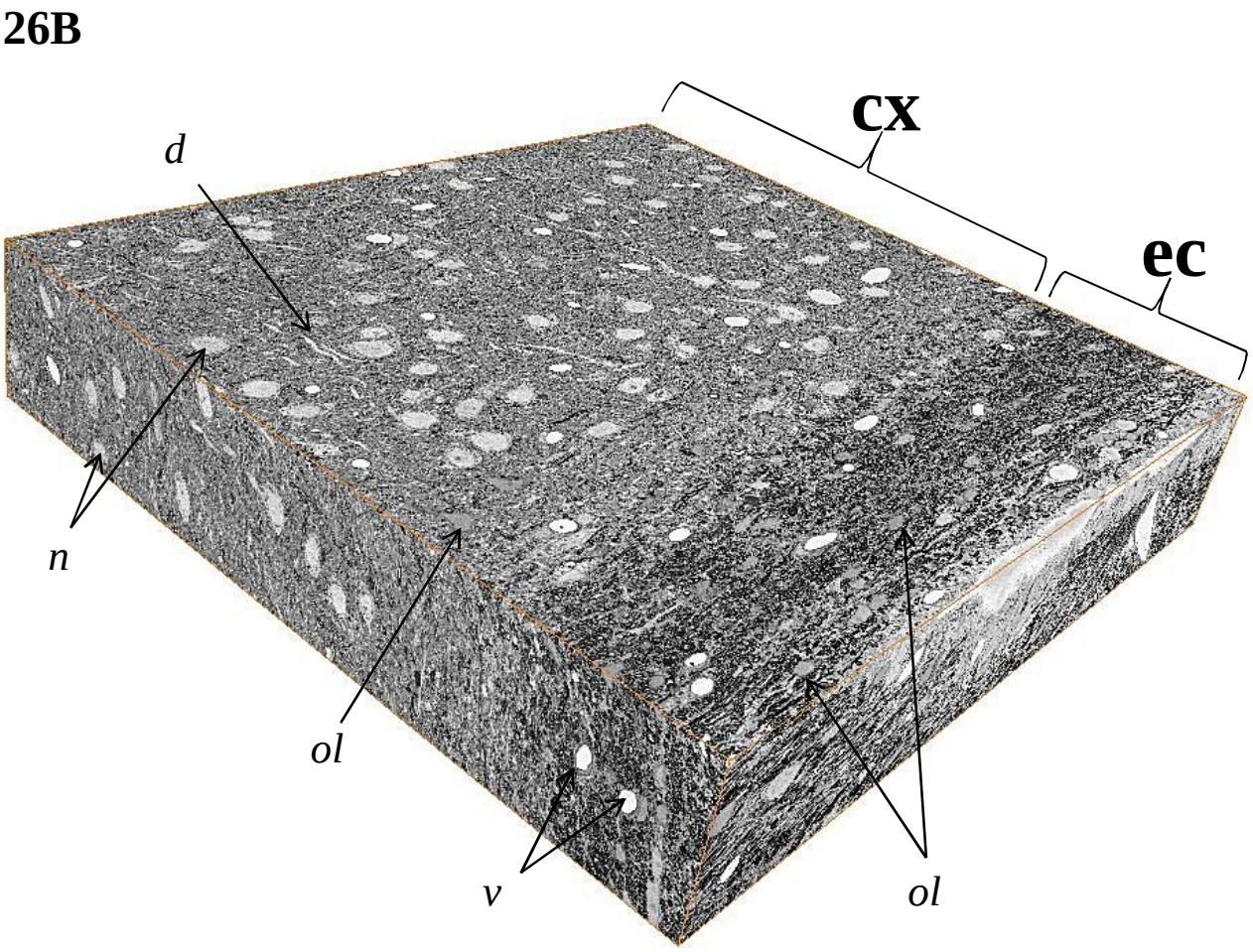


Fig. 26. 3D view of the SBEM blocks from the contralateral (A) and ipsilateral (B) cortex of a TBI rat. Abbreviations: cx, cortex; d, dendrite; ec, external capsule; n, neuron; ol, oligodendrocyte; v, vessel.

By looking at Fig. 26B, a huge decrease in the myelin sheath integrity and the number axons in the external capsule is noticeable. This white matter area also showed a loss of organization. In the cortex, more glial cells (presumably microglia) appeared to be present, associated with the loss of organization among dendrites and axons.

Fig. 27 shows 3D-FT analysis results from the cortex (Fig. 27A) and the external capsule (Fig. 27C). We found a decrease in anisotropy in the ipsilateral hemisphere as compared to

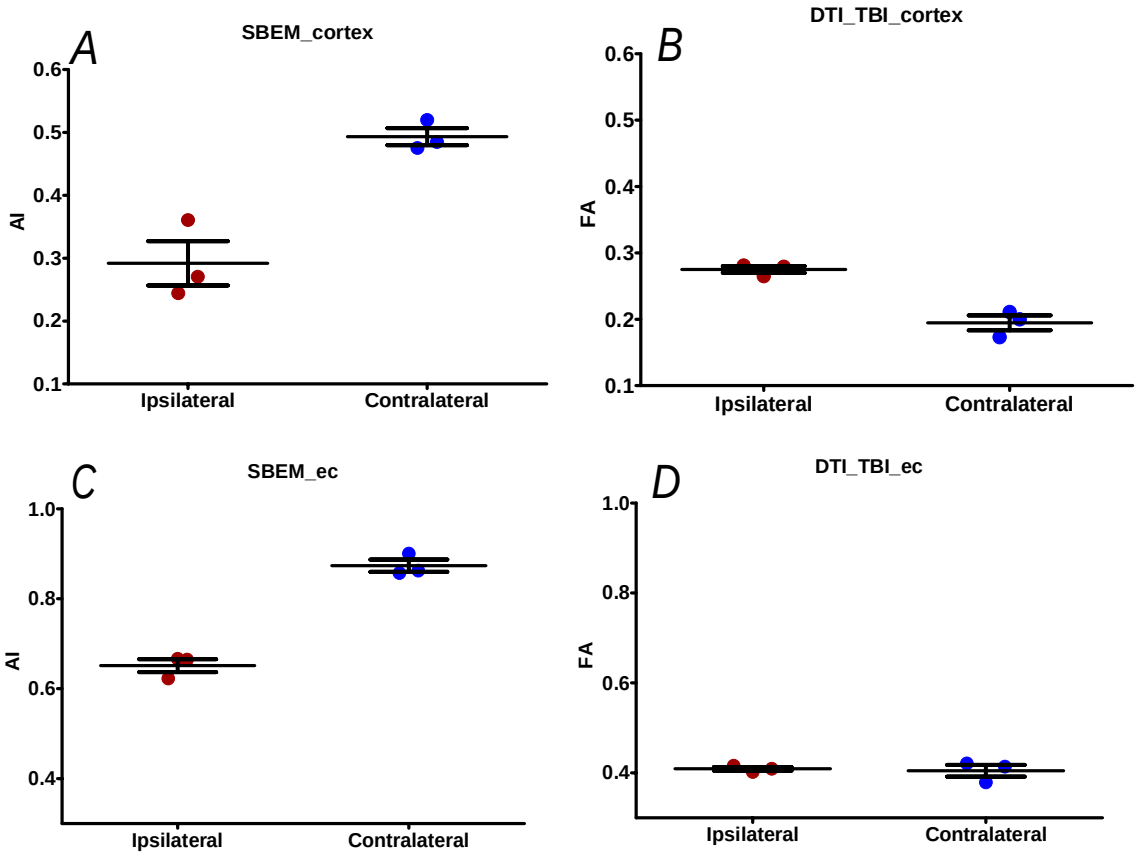


Fig. 27. Result for 3D-FT (A,C) and DTI (B,D) analyses of the cortex and external capsule. Graphs A,C show result of the average of 3 VOIs from one TBI rat, shown by a single dot. Each dot in graphs B,D represents the average of three voxels per each rat brain. Abbreviations: AI, anisotropy_3D; ec, external capsule; FA, fractional anisotropy.

contralateral hemisphere in both cortex and external capsule. These results matched with our observations (Fig. 26). However, DTI results did not show these differences in these two areas where values almost did not differ in the ipsilateral hemisphere as compared to contralateral hemisphere (Fig. 27B and 27 D). These could be explained by the partial volume effect when manually taking the voxels in the DTI maps. Those voxels might have contained portions of the external capsule and cortex, or vice versa which might alter the values within the voxel. Fig. 28 illustrates how the SBEM blocks differ from DTI, concerning the variance in the directionality in our data sources. When preparing tissue for SBEM, the brains were cut in the coronal plane in the same way it is shown for DTI in Fig. 25A and 25B. Thus, the data was obtained from DTI according to the same plane. However, the tissue´s reference in

the brain was lost during cutting further for SBEM preparation and staining (Fig. 28A). This was taken into consideration when analyzed the data from these brain areas in 3D-FT.

For comparing the orientations between the SBEM and DTI the variance between their Cartesian coordinates was used (Table 1).The following is an explanation of the presumptive angles in space based on three Cartesian components. Here the selection of voxels in DTI together with the challenge of describing the Cartesian angles are major limitations.

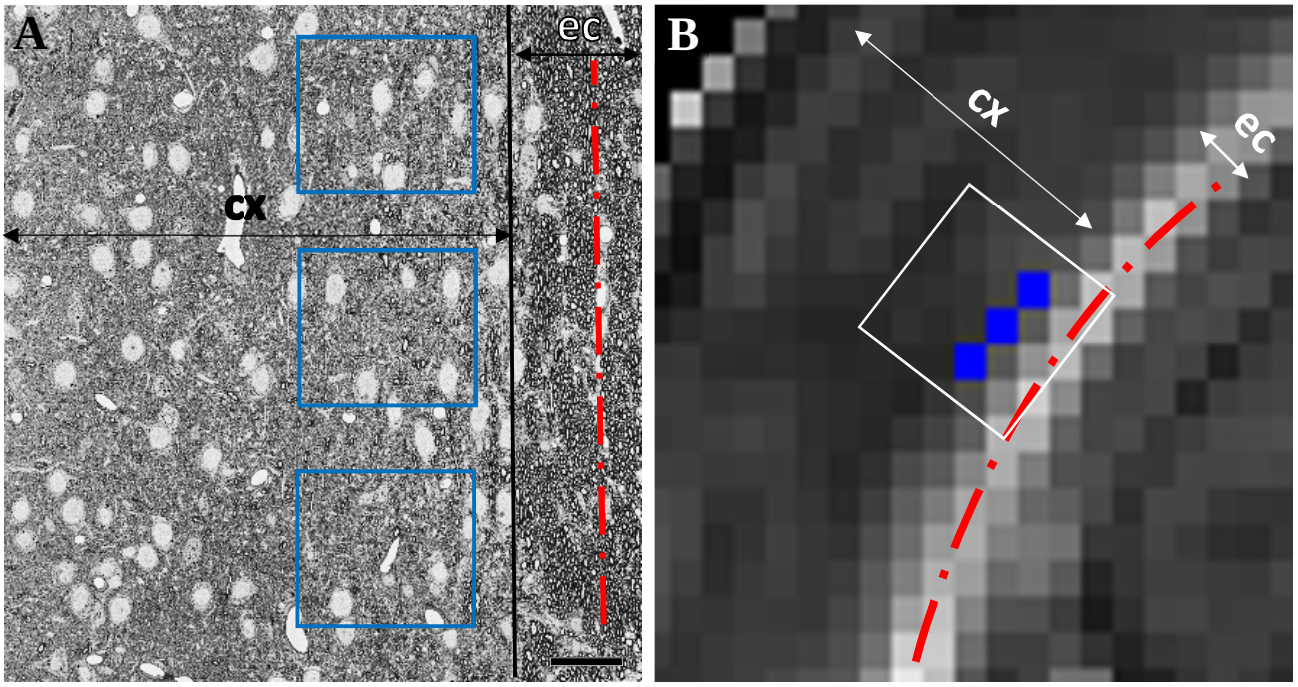


Fig. 28. The difference in directionality between SBEM and DTI indicated by the dashed red lines in the external capsule. Double arrows show the extent of the external capsule (white matter) and cortex (grey matter) (see Fig.24). A) One image of the contralateral cortex of the TBI rat. Scale bar = 36.8 µm. B) FA map of the same animal in the same side which is leaned regarding the above image. Each square elements in this image is a voxel, that has a grey scale intensity to indicate the overall anisotropy of all the numerous fibers included in that small voxel. The white square is approximately the whole EM-image (A), however rotated approximately for 45 degrees. The VOIs used for analysis are visible in blue squares in A,B. cx: cortex. ec: external capsule.

| EM-TBI-cl | X | Y | Z |
|---|---|---|---|
| VOI_1 | 0.1608 | 0.4551 | **0.8758** |
| VOI_2 | 0.1978 | 0.4813 | **0.8539** |
| VOI_3 | 0.1834 | 0.4517 | **0.8731** |
| VOI_4 | 0.0887 | 0.0151 | **0.9959** |
| VOI_5 | 0.0773 | 0.2013 | **0.9765** |
| VOI_6 | 0.0829 | 0.0878 | **0.9927** |
| Average | 0.132 | 0.282 | 0.928 |

| DTI-CX | X | Y | Z |
|---|---|---|---|
| 1 | 0.327 | 0.473 | **0.816** |
| 3 | 0.158 | **0.768** | 0.614 |
| 4 | **0.755** | 0.019 | 0.654 |
| 5 | 0.631 | 0.266 | **0.726** |

Table 1. Cartesian coordinates values obtained from the analyzed VOIs for cortex after TBI. Left: contralateral hemisphere of SBEM for six volumes of interest from one animal. Right: in DTI for five different brains (each row represents one rat).The bold numbers show the dominance of a particular Cartesian component, exhibiting the variance in manual selection of the voxels as volumes of interest. cl, contralateral, CX, cortex, DTI, diffusion tensor imaging, TBI, traumatic brain injury.

DTI analysis in the TBI cortex appeared to have varying orientations and did not indicate a distinct pattern in directionality as in SBEM. As it is shown in the right side of table 1,the orientation of animal 1 was slightly out of perpendicularity by the effect of the *Y* component whereas in animal number 4, *X* component created this deviating effect. Animal number 3 had a negligible *Y* component with an orientation in *X*-*Z* plane slightly leaning towards *X* direction. Animal number 2 had a major Y directionality but the secondary effect of *Z* made its orientation tilted towards *Z* axis. However, for animal number 3, the directionality was tilted toward the *Z* axis. The overall *Z* was either the first or second major component revealing a tilted orientation towards the reference plane *X*-*Y* (Table 1, right).

## 6. DISCUSSION

DTI is a remarkable tool for the detection of microstructural abnormalities during pathological processes. Understanding the DTI contrast is still under investigation. Due to being significantly sensitive to microstructural tissue changes, DTI has a great significance in clinical research of human brain (Wedeen et al., 2005; Mac Donald et al., 2007; Sidaros et al., 2008). There is also increasing demand in investigating the impact of pathological conditions on DTI anisotropy and fiber orientation (Assaf et al., 2003; Concha et al., 2006; Bartsch et al., 2012). The optimal purpose of analyses for determining the anisotropy is to reveal the changes in tissue directionality which, in turn, originates from a dominant orientation (Chetverikov and Haralick, 1995).

Anisotropic diffusion is caused by a higher molecular displacement of water along the coherently-oriented cylindrical morphologies involving axons (Beaulieu, 2002). As brain development completes, the lipid membranes of myelinated axons reach to their maximum growth. Thus, the water diffusion orthogonal to these fibers is highly hindered (Nomura et al., 1994). Some previous studies argued that myelinated membranes were not the unequivocal factor in determining the anisotropy (Beaulieu and Allen, 1994). However, among the more isotropically-orientend fibers of grey matter, DTI has been proved insufficient to estimate the directionality.

The lack of third dimension has been the main obstacle among the majority of previous efforts for the characterization of the three-dimensional DTI. Mostly, this has been done using the conventional histological preparations in healthy brain and during pathology. In this project, first we explored the possibilities of the 2D-FT analysis in conventional histological stainings. We investigated how two different components contributed to the water diffusion in control and pilocarpine rats in the corpus callosum, cortex and CA3b of the hippocampus. Then, we further developed 3D-FT and we hypothesized that Fourier transformation can be applied to the stacks of SBEM in order to generate anisotropy and orientation of the dominant fibers. In these stacks, all the microstructural components or membranes responsible of the water diffusion could be taken into account. Our results indicate that 2D-FT is an optimal method to analyze the conventional histological sections. This could be used for the investigation of individual components affecting the water diffusion. 3D-FT implemented in this work is a step forward in characterization of the DTI contrast by adding the 3$^{rd}$ dimension. Our results demonstrate that Fourier analysis in SBEM stacks of images provides fair values in 3D which can be directly correlated to DTI data and the hypothesis is accepted.

**Probabilistic algorithms and estimation methods for resolving the restrictions of DTI**

Since DTI is not reliable in determining the anisotropy of multiple fiber structures, several attempts have been focused on elevating the voxel resolution. High angular resolution diffusion imaging (HARDI) has been proposed to acquire diffusion measurements with fewer voxels that contain multiple fiber directions (Alexander et al., 2002). By the use of a

spherical coordinate system it was further optimized to reflect anisotropy of such voxels more accurately (Frank, 2001, 2002). Spherical deconvolution is also been used to help generate more efficient estimations of HARDI acquisitions without any primary assumptions about the number of fiber orientations (Tournier et al., 2004).

A combination of the composite-hindered and restricted model of diffusion MRI was theoretically developed to resolve the hindered and restricted diffusion of water molecules in the white matter (Assaf et al., 2004). It was further applied to human brain *in vivo*, aimed to provide an unbiased 3D quantification of the diffusion measurements and revealed a superb sensitivity to white matter abnormalities compared to DTI (Assaf and Basser, 2005).

Substantial efforts have been devoted to resolving the shortcomings of DTI by proposing *q*-space and Q-ball imaging methods (Tuch, 2004; Hess et al., 2006; Khachaturian et al., 2007). A contrast driven between uniaxial and planar models for diffusion tensor was performed by Wiegel and coworkers, based on the variance of the medium and minor eigenvalues for resolving crossing fiber patterns in DTI (Wiegel et al., 2000). To elaborate more, if the absolute value of the subtraction of two smaller eigenvalues is not negligible, the diffusion will be presented as planar in contrast to uniaxial. Nevertheless, neither of the two models proved to be capable of resolving the heterogeneous fiber orientations.

Diffusion spectrum imaging (DSI) is a method capable of estimating the density spectra of an incoherent organization within a voxel, a solution to the restrictions of DTI-based tractography (Wedeen et al., 2008). DSI is a powerful tool not only for the white matter´s crossing fibers but also in the grey matter, as it was observed in the same work in the cerebral cortex of the monkey *ex vivo*. It is worth mentioning that the Fourier transformation had been used in this method for a reconstruction of the original fiber density gained from the signal modulus (Wedeen et al., 2005).

**Further steps in the characterization of DTI contrast**

DTI assumes a Gaussian distribution of water displacement due to the diffusion. This creates limitations when the intravoxel information is needed to be extracted. For this goal, more advanced methods have been developed (as described in section 1.3.2). White *et al.*, 2013, developed restriction spectrum imaging (RSI) using the high *b*-value Cartesian *q*-space data on a tissue sample from the rat brain. Their method comprised the extension of the spherical

deconvolution model for HARDI acquisitions, in order to explore fiber orientations on a spectrum of length scales. The diffusion orientation was restated as a linear mixture of the symmetrical Gaussian response functions in a cylindrical exhibition. In other words, it is a linear reconstruction and modelling framework for multidirectional and multi *b*-value diffusion data. This helped resolving not only the length scale but the orientation information of the tissue microstructure in biological media. Thus compared to DSI, RSI reconstructions helped estimate a more detailed quantitative characterization in normal and pathological conditions. It was demonstrated that RSI can make a distinction between the volume fraction and orientation of the fine and coarse scale diffusion processes in the tissue of rat brain. This originates from the restricted and hindered diffusions in the intraneurite and extraneurite water compartments, respectively. The work done by Frank introduced a new transformation for characterization of anisotropy in HARDI, in a way that it could be decomposed to multi-fiber components. However, assuming the integral fibers as identical or non-existing exchange among fibers were pitfalls of this method (Frank, 2002).

The neural fiber orientation distributions gained from *ex vivo* diffusion MRI was developed by Leergaard *et al.*, 2010, aiming to estimate the microstructural organization of fibers. They were compared against histological measurements in the rat brain, by means of co-registration with the affine transformations. This method involved tracing the myelin fiber orientations as vectors. They utilized manual recordings of myelin stained tissues in the mediolaterally oriented fibers of the corpus callosum and transversely oriented bundles of the superior colliculus. Furthermore, they overlaid reconstructions on a gray scale FA map derived from the diffusion tensor (DT) eigenvalues. They showed that low FA values and disk-like DT profiles indicated the properties of crossing fibers, whereas high FA and elongated DT profiles were typically regarded as characteristics of the coherent fibers.

**2D-FT analysis in histological preparations**

We successfully implemented, improved and tested 2D-FT analysis in 2D histological preparations. We obtained significant differences only in one of our selected areas, CA3b in the hippocampus after status epilepticus. In the corpus callosum and in layer VI of the cortex, no differences were found between animals treated with pilocarpine and control animals, even if we had visually observed some changes in the histological sections. Moreover, when

we quantified anisotropy and orientation from those two areas using 2D-FT, we obtained only minor differences which were not significantly different from the controls. This could stem from the fact that the microstructural changes observed in the corpus callosum and the cortex were within the detection level of our method. In addition, other possible factors might be that some of these changes had opposite directions and they could have compensated each other.

Clinical studies have already found significantly reduced FA in orthogonal direction to the axons of epileptic patients in the external capsule and posterior corpus callosum (Arfanakis et al., 2002 a). Eriksson and collaborators focused on the malformations during cortical development as a contributor to epilepsy and discovered declined FAs among epilepsy patients with agenesis of the corpus callosum (Eriksson et al., 2001). At the initial progress of many CNS diseases, a change in the shape of astrocytes occurs involving a surge in GFAP expression in their components (Oberheim et al., 2008). Detecting these alterations in astrocytes following status epilepticus is very important for future therapeutic purposes. According to the findings of Wilhemsson and collaborators, in the cortex and hippocampus, reactive astrocytes increase the thickness of their molecular processes (Wilhelmsson et al., 2006). The morphology of astrocytes has been perceived as isotropic so that their growth would not be affecting or depressing the calculated anisotropy (Budde et al., 2011). However, we observed a significant increase in anisotropy of the reactive astrocytes and myelinated axons of CA3b by 52% and 46%, respectively. This was associated with a marked growth of astrocytes and to a lesser extent, plastic changes in myelinated axons. However, astrocytes appeared to have a greater role in increasing anisotropy after status epilepticus, presumably due to a coherent growth of their processes. In this region, the orientation degree increased by 29% in GFAP stained sections, and 137% in myelin stained sections. Budde and collaborators who aimed to identify cellular morphologies involved in the elevated anisotropy, found a similar pattern for GFAP in the cortex. Although DTI indicated increased anisotropy after status epilepticus in CA3b, it was not a significant change. This can be explained by the inability of DTI to detect complex fibers especially in the grey matter.

In the corpus callosum histology showed a decrease in anisotropy after status epilepticus both for myelin and GFAP stained sections, whereas DTI showed a slight increase in FA. It bears

resemblance to the previous clinical studies of epilepsy patients that observed significant reductions of FA in the corpus callosum (Arfanakis et al.,2002 a ; Thivard et al., 2005; Gross et al., 2006; Concha et al., 2006; Liu et al., 2011; Andrade et al., 2014). The projection of DTI eigenvectors through *Z* plane created a similar degree of orientation with histology in the corpus callosum, but this phenomenon did not occur in CA3b or cortex. In other words, DTI projection is not consistent with the 2D-FT orientations in grey matter. The consistency of the DTI projected orientations with myelinated axons in the white matter seems to be due to the distinct pattern of cohesively oriented fibers in a way that their projection creates the same 2D left-right directionality.

An advanced method as an alternative to 2D-FT anisotropy was also introduced by Budde and Frank, 2012 using the high resolution confocal microscopy. They argued that there was not a specifically standard method available for the validation of local tissue structures derived from the multi-fiber diffusion MRI. In order to find a solution, they developed an automated and quantitative method named as structure tensor (ST) analysis for the Dil-stained images of rat brain. Since ST is limited to 2D, the influence of through-plane fibers on the resulting images was also examined. Their results showed the predominant orientation of fibers in the rat cortex was perpendicular to the cortical surface. However, they argued that ST analysis had one major restriction which was the 2D nature of the histological sections.

**3D-FT analysis in SBEM stacks**

Owing to the high resolution of SBEM (0.28 $\mu m^3$) which is within the range of lipid membranes of myelinated axons, we were able to infer the barriers of the water diffusion in normal and in pathological conditions. The anisotropy generated from 3D-FT analysis of the corpus callosum in a control was as the same level as FA in DTI. In view of the highly anisotropic nature of the corpus callosum, it was expected to see a close correlation between SBEM and DTI. We discovered that Fourier analysis in the corpus callosum creates more precise results with bigger VOI dimensions. It is worth mentioning that the estimation of anisotropy from the power spectrum of the Fourier analysis is merely valid over large scales (Germain et al., 2003).

Previous clinical studies on patients with TBI have shown reductions in FA of the white matter fibers (Edlow et al., 2016). One longitudinal study found a remarkable decrease in FA among the body of the corpus callosum and external capsule of these patients compared to controls, after 11 weeks of follow up scans (Sidaros et al., 2008). Mac Donald and coworkers focused on traumatic axonal injury of mice and discovered a decrease in the relative anisotropy of DTI in the corpus callosum and the external capsule. In addition, they surprisingly discovered the presence of reactive astrocytes after the trauma by GFAP immunostaining, which did not appear in white matter of control subjects (Mac Donald et al., 2007). Arfanakis and colleagues found a significant decrease in FA of TBI patients in the corpus callosum and the external capsule during the one month follow up (Arfanakis et al., 2002 b).

We applied 3D-FT to cortex of a TBI rat and synonymous to Budde et.al, 2011, we found that the decrease in anisotropy in the ipsilateral hemisphere was associated with axonal degeneration and loss of myelin integrity. Moreover, we observed a decrease in anisotropy in the ipsilateral cortex compared to contralateral, associated with a distinguishable increase in the number of glial cells. The shape and the processes of these cells might be the reason for the changes in the parameters obtained from both analyses. Although 3D-FT showed a decrease in anisotropy on the ipsilateral cortex and external capsule, as compared to the contralateral, FA from DTI in both areas did not show any differences. As mentioned earlier, these could be explained by the partial volume effect of the voxels in the DTI maps (Vos et al., 2011).

Further work is necessary to solve the problems we faced in this project. For instance, the presence of geometric distortions due to tissue preparation, such as staining or cutting by the microtome, cannot be avoided precisely (McCulloch, 1965; Towe and Hamilton, 1968).
Artifacts attributable to the non-homogeneous stainings that lead to an increased signal to noise ratio should be avoided (Tsai et al., 2013). Anisotropy and orientation values for SBEM analysis by Fourier transformation can result in great variance based on the magnitude of the VOI block. Particularly in corpus callosum, the voxel magnitudes of our larger VOIs were not symmetrical. Thus, it is necessary to analyze a square cubic VOI in order to evaluate the differences it might make. Having cut the SBEM tissue inconsistently with the DTI reference,

we observed a disparity between the resulted orientations. For future experiments, registration methods between SBEM and DTI should be implemented to avoid this problem. However, the findings in this project are significant for a precise and realistic approach in DTI characterization and can further be expanded for other areas of brain research.

## 7. CONCLUSION

We efficaciously implemented a three-dimensional Fourier analysis to the 3D stacks of SBEM. This is a significant breakthrough in the evolution of DTI characterization and will contribute to a far better understanding of the DTI contrast. We also successfully applied 2D-FT to myelin and GFAP stained micrographs of grey and white matter for the status epilepticus rats to provide supplementary data for DTI characterization. Direct quantification of SBEM stacked images helps determine the underlying microstructural components of the brain tissues with cutting-edge resolution.

## 8. ACKNOWLEDGEMENTS

I would like to thank Dr. Alejandra Sierra and M.Sc. Raimo Salo for their leadership and support for this project, and Professors Olli Gröhn and Jonh Eriksson for giving me the opportunity to experience in A.I. Virtanen institute for molecular sciences of the University of Eastern Finland.

## 9. REFERENCES

Alexander, A., Lee, J., Lazar, M., and A., Field. Diffusion Tensor Imaging of the Brain. 2007. *Neurotherapeutics* 4: 316–329.

Alexander, D.C., Barker, G.J., Arridge, S.R. 2002.Detection and modeling of non-Gaussian apparent diffusion coefficient profiles in human brain data. *Magnetic Resonance in Medicine* 48:331–340.

Anderson, W. 2005. Measurement of Fiber Orientation Distributions Using High Angular Resolution Diffusion Imaging. *Magnetic Resonance in Medicine* 54:1194–1206.

Andrade ,C.S., Leite, C.C., Otaduy, M.C.G., Lyra, K.P. , Valente, K.D.R., Yasuda C. L., Beltramini, G.C., Beaulieu, C., Gross, D.W. 2014. Diffusion abnormalities of the corpus

callosum in patients with malformations of cortical development and epilepsy. *Epilepsy Research* 108: 1533-1542.

Arfanakis, K., Haughton, V.M., Carew, J.D., Rogers, B.P., Dempsey, R.J., and Meyerand, M.E. 2002 (b). Diffusion Tensor MR Imaging in Diffuse Axonal Injury. *AJNR* 23:794–802.

Arfanakis, K., Hermann, B.P., Rogers, B.P., Carew, J.D., Seidenberg, M., Meyerand, M.E. 2002 (a). Diffusion tensor MRI in temporal lobe epilepsy. *Magnetic Resonance Imaging* 20: 511–519.

Assaf, B.A., Mohamed, F.B., Abou-Khaled, K.J., Williams, J.M., Yazeji, M.S., Haselgrove, J., and Faro, S.H. 2003. Diffusion Tensor Imaging of the Hippocampal Formation in Temporal Lobe Epilepsy. *AJNR* 24:1857–1862.

Assaf, Y., and Basser, P.J.2005.Composite hindered and restricted model of diffusion (CHARMED) MR imaging of the human brain. *Neuroimage* 27:48-58.

Assaf, Y., Freidlin, R.Z., Rohde, G.K., Basser, P.J. 2004. New modeling and experimental framework to characterize hindered and restricted water diffusion in brain white matter. *Magnetic Resonance in Medicine* 52:965-78.

Axer, H., Beck, S., Axer, M., Schuchardt F., Heepe J., Flücken A., Axer M., Prescher A., and Witte, O.W. 2011(a).Microstructural analysis of human white matter architecture using polarized light imaging: views from neuroanatomy. *Frontiers in Neuroinformatics* 5, Article 28.

Axer, H., and Keyserlingk, D.G. 2000. Mapping of fiber orientation in human internal capsule by means of polarized light and confocal scanning laser microscopy. *Journal of Neuroscience Methods* 94:165–175.

Axer, H., Lippitz, B.E., Keyserlingk, D.G. 1999. Morphological asymmetry in anterior limb of human internal capsule revealed by confocal laser and polarized light microscopy. *Psychiatry Research: Neuroimaging Section* 91:141-154.

Axer, M., Amunts, K., Grässel, D., Palm, C., Dammers, J., Axer, H., Pietrzyk, U., Zilles, K. 2011 (b). A novel approach to the human connectome: Ultra-high resolution mapping of fiber tracts in the brain. *Neuroimage* 54: 1091–1101.

Ayres, C.E., Jha, B.S., Meredith, H., Bowman, J.R., Bowlin, G.L., Scott, C., Henderson, S.C., Simpson, D.G. 2008. Measuring fiber alignment in electrospun scaffolds: a user's guide to the 2D fast Fourier transform approach. *Journal of Biomaterial Science*, Polymer Edition 19: 603–621.

Bartsch, H., Maechler, P., and Annese, J. 2012. Automated Determination of Axonal Orientation in the Deep White Matter of the Human Brain. *Brain Connectivity* 2: 284-290.

Basser, P.J., and Pajevic, S. 2000. Statistical artifacts in diffusion Tensor MRI caused by background noise. *Magnetic Resonance in Medicine* 44: 41-50.

Basser, P.J., and Jones, D.K. 2002. Diffusion tensor MRI: theory, experimental design and data analysis- a technical review. *NMR in Biomedicine* 15:456-467.

Basser, P.J., and Pierpaoli, C. 1996. Microstructural and Physiological Features of Tissues Elucidated by Quantitative-Diffusion-Tensor MRI. *Journal of Magnetic Resonance*, Series B 111: 209–219.

Basser, P.J., Mattiello, J., Le Bihan, D. 1994. Estimation of the effective self-diffusion tensor from NMR spin echo. *Journal of Magnetic Resonance* 103:247-254.

Bear, M., F., Connors, B., W., and M., A., Paradiso. 2007. Neuroscience, exploring the brain. Third edition. Lippincott Williams & Wilkins, 2007, 857 pp.

Beaulieu, C. 2002.The basics of anisotropic water diffusion in the nervous system, a technical review. *NMR in Biomedicine* 15:435–455.

Beaulieu, C., Allen, P.S. 1994. Determinants of anisotropic water diffusion in nerves. *Magnetic Resonance in Medicine* 4:394-400.

Benson, R.R., Gattu, R., Sewick, B., Kou, Z., Zakariah, N., Cavanaugh, J., M., Haacke, E. M. 2012. Detection of hemorrhagic and axonal pathology in mild traumatic brain injury using advanced MRI: Implications for neurorehabilitation. *Neurorehabilitation* 31: 261-279.

Borrett, S., and L., Hughes. 2016. Reporting methods for processing and analysis of data from serial block face scanning electron microscopy. *Journal of Microscopy* 263: 3-9.

Budde, M.D., and J., Annese. 2013. Quantification of anisotropy and fiber orientation in human brain histological sections. *Frontiers in Integrative Neuroscience* 7, Article3.

Budde, M.D., Frank, J.A. 2012. Examining brain microstructure using structure tensor analysis of histological section. *Neuroimage* 63:1-10.

Budde, M.D., Janes, L., Gold, E., Turtzo, L.C., and Frank, J.A. 2011. The contribution of gliosis to diffusion tensor anisotropy and tractography following traumatic brain injury. *Brain* 134: 2248-2260.

Chetverikov, D., and R. M., Haralick. 1995. In: *Texture anisotropy, symmetry, regularity: recovering structure and orientation from interaction maps.* BMVA Press Surrey 1:57-66.

Concha, L., Gross, D. W., Wheatley, B., and C., Beaulieu. 2006. Diffusion tensor imaging of time-dependent axonal and myelin degradation after corpus callosotomy in epilepsy patients. *Neuroimage* 32: 1090 – 1099.

Denk, W., and Horstmann, H. 2004. Serial block-face scanning electron microscopy to reconstruct three-dimensional tissue nanostructure. *Plos Biology* 2(11). e329.

Denk, W., Briggman, K.L., and Helmstaedter, M. 2012. Structural neurobiology: missing link to a mechanistic understanding of neural computation. *Nature Reviews* 13:351-358.

Edlow, B.L., Copen, W.A., Izzy, S., Bakhadirov, K., Kouwe, A., Glenn, M.B., Greenberg, S.M., Greer, D.M., and Wu, O. 2016. Diffusion tensor imaging in acute-tosubacute traumatic brain injury: a longitudinal analysis. *BMC Neurology* 16:2.

Eriksson, S.H., Rugg-Gunn, F.J., Symms, M.R., Barker, G.J., Duncan, J.S. 2001. Diffusion tensor imaging in patients with epilepsy and malformations of cortical development. *Brain* 124:617-626.

Filippi, M., G. Comi, M. Rovaris. 2012. Springer Science & Business Media, Medical - 159 pp.

Frank, L.R. 2002. Characterization of Anisotropy in High Angular Resolution Diffusion-Weighted MRI. *Magnetic Resonance in Medicine* 47:1083–1099.

Frank, L.R.2001. Anisotropy in High Angular Resolution Diffusion-Weighted MRI. *Magnetic Resonance in Medicine* 45:935–939.

Germain, C., Da Costa, J.P., Lavialle, O., Baylou, P. 2003. Multiscale estimation of vector field anisotropy application to texture characterization. *Signal Processing* 83:1487-1503.

Gross, D. W., Concha, L., and Beaulieu, C.2006. Extratemporal White Matter Abnormalities in Mesial Temporal Lobe Epilepsy Demonstrated with Diffusion Tensor Imaging .*Epilepsia* 47:1360–1363.

Hess, C.P., Mukherjee, P., Han, E.T., Xu, D., Vigneron, D.B. 2006. Q-ball reconstruction of multimodal fiber orientations using the spherical harmonic basis. *Magnetic Resonance in Medicine* 56:104-17.

Husain, M., and J. M. Schott. Oxford Textbook of Cognitive Neurology and Dementia. Oxford University Press, 9. Jun. 2016. pp: 560.

Jespersen, S.N., Leigland, L.A., Cornea, A., and Kroenke, C.D. 2012. Determination of axonal and dendritic orientation distributions within the developing cerebral cortex by Diffusion Tensor Imaging. *IEEE Transactions on Medical Imaging* 31:16-32.

Josso, B., Burton, D.R., Lalor, M.J. 2005. Texture orientation and anisotropy calculation by Fourier transform and principal component analysis. *Mechanical Systems and Signal Processing* 19:1152-1161.

Khachaturian, M.H., Wisco, J.J., Tuch, D.S. 2007 .Boosting the sampling efficiency of q-Ball imaging using multiple wave vector fusion. *Magnetic Resonance in Medicine* 57:289-96.

Khan, A.R., Cornea, A., Leigland, L.A., Kohama, S.G., Jespersen, S.N., Kroenke, C.D. 2015. 3D structure tensor analysis of light microscopy data for validating diffusion MRI. *Neuroimage* 111:192–203.

Kharatishvili, I., Sierra, A., Immonen, R.J., Gröhn, O., and Pitkänen, A. 2009. Quantitative T2 mapping as a potential marker for the initial assessment of the severity of damage after traumatic brain injury in rat. *Experimental Neurology* 217: 154-164.

Kinnunen, K., R., Greenwood, J.,Powell, R.,Leech, P.,Hawkins,V., Bonnelle, M.,Patel,S., Counsell and D.,Sharp. 2010. White matter damage and cognitive impairment after traumatic brain injury. *Brain* 134(2): 449–463.

Kullkarni, P.M., Barton, E., Savelonas, M., Padmanabhan, R., Lu, Y., Trett, K., Shain, W., Leasure, J.L., Roysam, B. 2015. Quantitative 3-D analysis of GFAP labeled astrocytes from fluorescence confocal images. *Journal of Neuroscience Methods* 246:38–51.

Leergaard, T., White, N.S., Crespigny, A.D., Bolstad, I., D´Arceuil, H., Bjaalie J.G., Dale A.D. 2010. Quantitative histological validation of diffusion MRI fiber orientation distributions in the rat brain. *Plosone* 5(1): e8595.

Levitan, B.I., and Kaczmarek, L.K. The neuron: cell and molecular biology. Oxford University Press, 2002, 579 pp.

Lewis, D.A., Campbell, M.J., Morrison, J.H. 1986. An immunohistochemical characterization of somatostatin28 and somatostatin-281-12 in monkey prefrontal cortex. *Journal of Comparative Neurology* 248:1–18.

Li, J., Li, X.Y., Feng, D.F., Gu, L. 2011. Quantitative evaluation of microscopic injury with diffusion tensor imaging in a rat model of diffuse axonal injury. *The European Journal of Neuroscience* 33: 933-45.

Lichtman, J.W., Pfister, H., and N., Shavit. 2014. The big data challenges of connectomics. *Nature Neuroscience* 17: 1448–1454.

Liu, M., Concha, L., Beaulieu, C., and D.W., Gross. 2011. Distinct white matter abnormalities in different idiopathic generalized epilepsy syndromes. *Epilepsia* 52:2267–2275.

Longstaff, A. Neuroscience. Garland Science, 2000, Medical. BIOS scientific publishers, 436 pp.

Mac Donald, C.L., Dikranian, K., Bayly, P., Holtzman, D., and Brody, D. 2007. Diffusion Tensor Imaging Reliably Detects Experimental Traumatic Axonal Injury and Indicates Approximate Time of Injury. *The Journal of Neuroscience* 27: 11869–11876.

Mädler, B., Drabycz, S.A., Kolind, S. H., Whittall, K.P., and A.L., MacKay. 2008. Is diffusion anisotropy an accurate monitor of myelination? Correlation of multicomponent T2 relaxation and diffusion tensor anisotropy in human brain. *Magnetic Resonance Imaging* 26:874–888.

Marquez, J.P. 2006. Fourier analysis and automated measurement of cell and fiber angular orientation distributions. *International Journal of Solids and Structures* 43: 6413–6423.

Matsushita, M., Hosoda, K., Naitoh, Y., Yamashita, H., and E., Kohmura. 2011. Utility of diffusion tensor imaging in the acute stage of mild to moderate traumatic brain injury for detecting white matter lesions and predicting long-term cognitive function in adults. *Journal of Neurosurgery* 115:130–139.

McCulloch, J.R.1965. Three-Dimensional ultramicrotomy: A new electron microscopic technique. *Journal of Ultrastructure Research* 13: 34-37.

Menzel, M., Michielsen, K., De Raedt, H., Reckfort, J., Amunts, K., and Axer, M. 2015. A Jones matrix formalism for simulating three-dimensional polarized light imaging of brain tissue. *Journal of Royal Society Interface* 12: 111.

Mikula, S., Binding J., and W., Denk. 2012. Staining and embedding the whole mouse brain for electron microscopy. *Nature Methods* 9: 1198-1201.

Miranda, K., Girard-Dias, W., Attias, M., De Souza, W., and I., Ramos. 2015. Three Dimensional Reconstruction by Electron Microscopy in the Life Sciences: An introduction for Cell and Tissue Biologists. *Molecular Reproduction & Development* 82:530–547.

Mori S, Tournier J-D. Introduction to diffusion tensor imaging and higher order models. 2nd ed. Burlington: Elsevier Science, 2014. 141 p.

Moseley, M., Kucharczyhka, J., Asgari, H.S., and Norman, D. 1991. Anisotropy in Diffusion-Weighted MRI. *Magnetic Resonance in Medicine* 19: 321-326.

Moseley, M.E., Cohen, Y.C., Kucharczyk, J., Asgari, H.S., Wendland, M.F., Tsuruda, J., Norman, D. 1990. Diffusion-weighted MR imaging of anisotropic water diffusion in cat central nervous system. *Radiology* 176: 439–445.

Napadow, V.J., Chen, Q., Mai, V., So, P. T. C., and Gilbert, R.J. 2001. Quantitative Analysis of Three-Dimensional-Resolved Fiber Architecture in Heterogeneous Skeletal Muscle Tissue Using NMR and Optical Imaging Methods. *Biophysical Journal* 80: 2968-2975.

Nilsson, M., van Westen, D., Ståhlberg, F., Sundgren, P.C., Lätt, J. 2013. The role of tissue microstructure and water exchange in biophysical modelling of diffusion in white matter. *Magnetic Resonance Materials in Physics, Biology and Medicine* 26:345–370.

Nomura, Y., Sakuma, H., Takeda, K., Tagami, T., Okuda Y., and Nakagawa, T.1994. Diffusional Anisotropy of the Human Brain Assessed with Diffusion Weighted. American *Journal of Neuroradialogy* 15: 231-238.

Oberheim, N.A., Tian, G., Han, X., Peng, W., Takano, T., Ransom, B., and Nedergaard, M. 2008. Loss of Astrocytic Domain Organization in the Epileptic Brain. *The Journal of Neuroscience* 28: 3264-3276.

Petroll, W.M., and Robertson, D.M. 2015. In Vivo Confocal Microscopy of the Cornea: New Developments in Image Acquisition, Reconstruction, and Analysis Using the HRT-Rostock Corneal Module. *The Ocular Surface* 13:187-203.

Reckfort, J., Wiese, H., Pietrzyk, U., Zilles, K., Amunts, K., and Axer, M. 2015. A multiscale approach for the reconstruction of the fiber architecture of the human brain based on 3D-PLI. *Frontiers in Neuroanatomy* 9:118.

Rodríguez-Cruces, R., and Concha, L. 2015 .White matter in temporal lobe epilepsy: clinico-pathological correlates of water diffusion abnormalities. *Quantitative Imaging in Medicine and Surgery* 5: 264-278.

Rutgers, D.R., Toulgoat, F., Cazejust, J., Fillard, P., Lasjaunias, P., and D., Ducreux. 2008. White Matter Abnormalities in Mild Traumatic Brain Injury: A Diffusion Tensor Imaging Study. *AJNR* 29:514-9.

Sawai, T., Kamataki, A., Uzuki, M., Ishida, K., Hanasaka, T., Ochi, K., Hashimoto, T., Kubo, T., Morikawa, A., Ochi, T., and K., Tohyama. 2013. Serial block-face scanning electron microscopy combined with double-axis electron beam tomography provides new insight into cellular relationships. *Microscopy* 62: 317–320.

Schilling, K., Janve, V., Gao,Y. , Stepniewska, I., Landman ,B.A., Anderson, A.W. 2016. Comparison of 3D orientation distribution functions measured with confocal microscopy and diffusion MRI. *Neuroimage* 129: 185–197.

Schrauwen, J.T.C., Vilanova, A., Rezakhaniha, R., Stergiopulos, N., van de Vosse, F.N., Bovendeerd, P.H.M. 2012. A method for the quantification of the pressure dependent 3D collagen configuration in the arterial adventitia. *Journal of Structural Biology* 180:335–342.

Seehaus, A., Roebroeck, A., Bastiani, M., Fonseca, L., Bratzke, H., Lori, N., Vilanova, A., Goebel, R., and R., Galuske. 2015. Histological validation of high-resolution DTI in human post mortem tissue. *Frontiers in Neuroanatomy* 9:98.

Sidaros, A., Engberg, A.W., Sidaros, K., Liptrot, M.G., Herning, M., Petersen, P., Paulson, O.B., Jernigan, T.L., and Rostrup, E. 2008. Diffusion tensor imaging during recovery from severe traumatic brain injury and relation to clinical outcome: a longitudinal study. *Brain* 131: 559 - 572.

Soares, J.M., Marques, P., Alves, V., and Sousa, N. 2013. A hitchhiker´s guide to diffusion tensor imaging. *Frontiers in Neuroscience* 7: 31.

Tardif , C., A., Schäfer , R.,Trampel , A., Villringer ,R.,Turner , P.,Bazin. 2016. Open Science CBS Neuroimaging Repository: Sharing ultra-high-field MR images of the brain. *Neuroimage* 124: 1143–1148.

Thai, T.Q., Nguyen, H. B., Saitoh, S., Wu, B., Saitoh, Y., Shimo, S., Hosny, Y., Elewa, A., Ichii, O., Kon, Y., Takaki, T., Joh, K., Ohno, N. 2016. Rapid specimen preparation to improve the throughput of electron microscopic volume imaging for three-dimensional analyses of subcellular ultrastructures with serial block-face scanning electron microscopy. *Medical Molecular Morphology* 49: 154-62.

Thivard, L., Lehericy, S., Krainik, A., Adam, C., Dormont, D., Chiras, J., Baulac, M., Dupont, S. 2005. Diffusion tensor imaging in medial temporal lobe epilepsy with hippocampal sclerosis. *Neuroimage* 28:682–690.

Tournier, J.D., Calamante, F., Gadian, D. G., and A., Connelly. 2004. Direct estimation of the fiber orientation density function from diffusion-weighted MRI data using spherical deconvolution. *Neuroimage* 23:1176– 1185.

Towe, K. M., and G.H., Hamilton. 1968. Ultramicrotome-induced deformation artifacts in densely calcified material. *Journal of Ultrastructure Research* 22:274-281.

Tsai, W.T., Hassan, A., Sarkar, P., Correa, J., Metlagel, Z., Jorgens, D.M., Auer, M. 2013. From voxels to knowledge: a practical guide to the segmentation of complex electron microscopy 3D-data. *Journal of Visualized Experiments* 90: e51673.

Tuch, D.S. 2004. Q-ball imaging. *Magnetic Resonance in Medicine* 52:1358-72.

Van Eijsden, P., Otte, W.M., van der Hel, W.S., van Nieuwenhuizen, O., Dijkhuizen, R.M., de Graaf, R.A., Braun, K.P. 2011. In vivo diffusion tensor imaging and ex vivo histologic characterization of white matter pathology in a post-status epilepticus model of temporal lobe epilepsy. *Epilepsia* 52:841-5.

Vos, S.B., Jones, D.K., Viergever, M.A., Leemans, A. 2011. Partial volume effect as a hidden covariate in DTI analyses. *Neuroimage* 55: 1566–1576.

Wedeen, V. J., Hagmann, P., Tseng, W.Y.I., Reese T.G., and R. M., Weisskoff. 2005. Mapping complex tissue architecture with diffusion spectrum magnetic resonance imaging. *Magnetic Resonance in Medicine* 54:1377–1386.

Wedeen, V. J., Wang, R.P., Schmahmann, J.D., Benner, T., Tseng, W.Y.I., Dai, G. Pandya, D.N., Hagmann, P., D'Arceuil, H., and A.J., de Crespigny. 2008. Diffusion spectrum magnetic resonance imaging (DSI) tractography of crossing fibers. *Neuroimage* 41:1267–1277.

Wernitznig, S., Sele, M., Urschler, M., Zankel, A., Polt, P., Rindd, F. C., Leitinger, G. 2016. Optimizing the 3D-reconstruction technique for serial block-face scanning electron microscopy. *Journal of Neuroscience Methods* 264: 16–24.

Werring, D. J., Clark, C. A., Barker, G. J., Miller, D. H., Parker, G. J. M., Brammer, M. J., Bullmore, E.T., Giampietro ,V.P., Thompson, A.J.1998. The structural and functional mechanisms of motor recovery: complementary use of diffusion tensor and functional magnetic resonance imaging in a traumatic injury of the internal capsule. *Journal of Neurology, Neurosurgery and Psychiatry* 65: 863-869.

White, N. S., Leergaard, T.B., D´Arceuil, H., Bjaalie, J.G., and Dale, A.M. 2013. Probing tissue microstructure with restriction spectrum imaging: histological and theoretical validation. *Human Brain Mapping* 34:327-346.

Wiegel, M.R., Larsson, H.B., Wedeen, V.J. 2000. Fiber crossing in human brain depicted with diffusion tensor MR imaging. *Radiology* 217: 897-903.

Wilhelmsson, U., Bushong, E.A., Price, D.L., Smarr, B.L., Phung, V., Terada, M., Ellisman, M.H., Pekny, M. 2006. Redefining the concept of reactive astrocytes as cells that remain within their unique domains upon reaction to injury. Proceedings of the National Academy of Sciences of the United States of America 103:17513-8.

Xu, J., Rasmussen, I., Lagopoulos, J., and A., Håberg. 2007. Diffuse Axonal Injury in Severe Traumatic Brain Injury Visualized Using High-Resolution Diffusion Tensor Imaging. *Journal of Neurotrauma* 24:753-65.

Zankel, A., Wagner, J., Poelt, P. 2014. Serial sectioning methods for 3D investigations in materials science. *Micron* 62: 66–78.

## Ø Appendix

A geometrical difference between default elevation angles Φ versus φ can be explained simply by the rules in trigonometry (see Fig.15).

The elevation angle of the spherical coordinate system is Φ however in Matlab it is defined as φ by default. It was required to rephrase this angle so that it would be compatible with the software:

$$\varphi + \Phi = \frac{\pi}{2}$$

In other words, Φand φ are supplementary angles:

$$\Phi = \frac{\pi}{2} - \varphi$$

As a result it can be concluded that:

$$\sin\left(\frac{\pi}{2} - \varphi\right) = \cos\varphi$$

Whereas:

$$\cos\left(\frac{\pi}{2} - \varphi\right) = \sin\varphi$$

The right triangle *DOP*:

$$\sin\Phi = \frac{|DP|}{r}$$

And we will have:

$$|DP| = r\sin\Phi$$

Similarly:

$$\cos\Phi = \frac{|OD|}{r}$$

This is rephrased as:

$$|OD| = r \cos \Phi$$

In the right triangle ΔAOB:

$$\sin \theta = \frac{|AB|}{r_{xy}}$$

Where $r_{xy}$ shown as a blue vector in Fig. 15, is the projection of r on x-y plane:

$$|AB| = r_{xy} \sin \theta$$

In the same way:

$$\cos \theta = \frac{|OA|}{r_{xy}}$$

And:

$$|OA| = r_{xy} \cos \theta$$

Projection of r through Φ towards the X axis forms the x component of the Cartesian system stated with spherical components:

$$x = r \sin \Phi \cos \theta$$

Which can be further restated with the $\varphi$:

$$x = r \cos \varphi \cos \theta$$

And similarly:

$$y = r \sin \Phi \sin \theta$$

That can be restated as:

$$y = r \cos \varphi \sin \theta$$

The projection of *r* to the *z* axis through the angle Φ:

$$z = r \cos \Phi$$

With the same procedure z can be rephrased with the angle $\varphi$:

$$z = r \sin \varphi$$